Supplementary Information

Nano-confinement Engineering Boosts C–N Coupling for Urea Electrosynthesis

Jiaxin Du,[1,2] Yunshuo Wu,[1,2] Siyu Fang,[1,2] Daliang Xu,[3] Min Liu,[4] Heng Liang,[3] Zhongbiao Wu[1,2,*] Gaoqing (Max) Lu,[5,6,*] Xuanhao Wu,[1,2,*]

[1] College of Environmental and Resources Science, Zhejiang University, Hangzhou, 310058, China
[2] Zhejiang Provincial Key Laboratory of Air Pollution Monitoring and Synergistic Control, Zhejiang University, Hangzhou, 310058, China
[3] State Key Laboratory of Urban Water Resource and Environment, School of Environment, Harbin Institute of Technology, Harbin, 150090, China
[4] State Key Laboratory of Powder Metallurgy, School of Physical and Electronics, Central South University, Changsha, 410083, China
[5] University of Surrey, GU2 7XH, Guildford, UK
[6] ARC Centre of Excellence for Functional Nanomaterials, University of Queensland, Brisbane, 4072, Australia
Corresponding authors: Zhongbiao Wu, E-mail: zbwu@zju.edu.cn; Gaoqing (Max) Lu, E-mail: maxlu@uq.edu.au; Xuanhao Wu, E-mail: xuanhao.wu@zju.edu.cn

Table of Contents

Supplementary Note 1

The acquired EXAFS data were processed according to the standard procedures using the ATHENA module of Demeter software packages. The spectra were energy-calibrated and normalized. The energy of the strongest peak of the first-order derivative of X-ray absorption near edge structure (XANES) is set to E0. The extended X-ray absorption fine structure (EXAFS) was extracted in k-space and Fourier transformed using the k3-weighted EXAFS function to amplify oscillations at high k-values. The detailed fitting parameters are shown in Table S4. The following EXAFS equation was used (Equation S1):

$$\chi(k) = \sum_j \frac{N_j S_0^2 F_j(k)}{kR_j^2} \cdot \exp\left[-2k^2\sigma_j^2\right] \cdot \exp\left[\frac{-2R_j}{\lambda(k)}\right] \cdot \sin\left[2kR_j + \phi_j(k)\right] \quad \text{(S1)}$$

the theoretical scattering amplitudes, phase shifts and the photoelectron mean free path for all paths were calculated. S_0^2 is the amplitude reduction factor, $F_j(k)$ is the effective curved-wave backscattering amplitude, N_j is the number of neighbors in the j^{th} atomic shell, R_j is the distance between the Xray absorbing central atom and the atoms in the j^{th} atomic shell (back scatterer), λ is the mean free path in Å, $\phi_j(k)$ is the phase shift (including the phase shift for each shell and the total central atom phase shift), σ_j is the Debye-Waller parameter of the j^{th} atomic shell (variation of distances around the average R_j). The functions $F_j(k)$, λ and $\phi_j(k)$ were calculated with the ab initio code FEFF10.

Supplementary Note 2

Nernst-Planck equations:

$$J_i = D_i\left(\nabla c_i + \frac{z_i F c_i}{RT}\nabla\varphi\right) + c_i u \quad \text{(S2)}$$

where J_i represents the current density of the electrode, D_i is the diffusion coefficient (Table S14), ∇c_i is the concentration gradient, z_i is the current density, F represents the Faraday constant (96485.34 C mol^{-1}), R represents the ideal gas constant (8.3145 J mol^{-1} K^{-1}), T represents the temperature in Kelvin (293.15 K), $\nabla\varphi$ is the potential difference and u is the fluid velocity.

Fick's Rule:

$$N_i = -D_i \nabla c_i \quad \text{(S3)}$$

where N_i represents the diffusion flux.

Tafel equation:

$$i = i_0 \exp\left(\frac{\alpha n F \eta}{RT}\right) \quad \text{(S4)}$$

where i_0 represents the exchange current density, α is the charge transfer coefficient, n is the number of electrons transferred, η is the overpotential.

The diffusion coefficient (D, m^2 s^{-1}) of urea calculation. (Equation S5 and S6)[1]:

$$MSD = \frac{1}{N}\sum_{1}^{N} \{[r(t) - r(0)]^2\} \text{ (S5)}$$

$$D = \frac{1}{6} \lim_{N\to\infty} \frac{d}{dx}\{[r(t) - r(0)]^2\} \text{ (S6)}$$

where N is the total number of the targeted molecule (urea), $r(0)$ and $r(t)$ represent the initial position (m) and position at t (m) of the targeted molecule.

Supplementary Figures

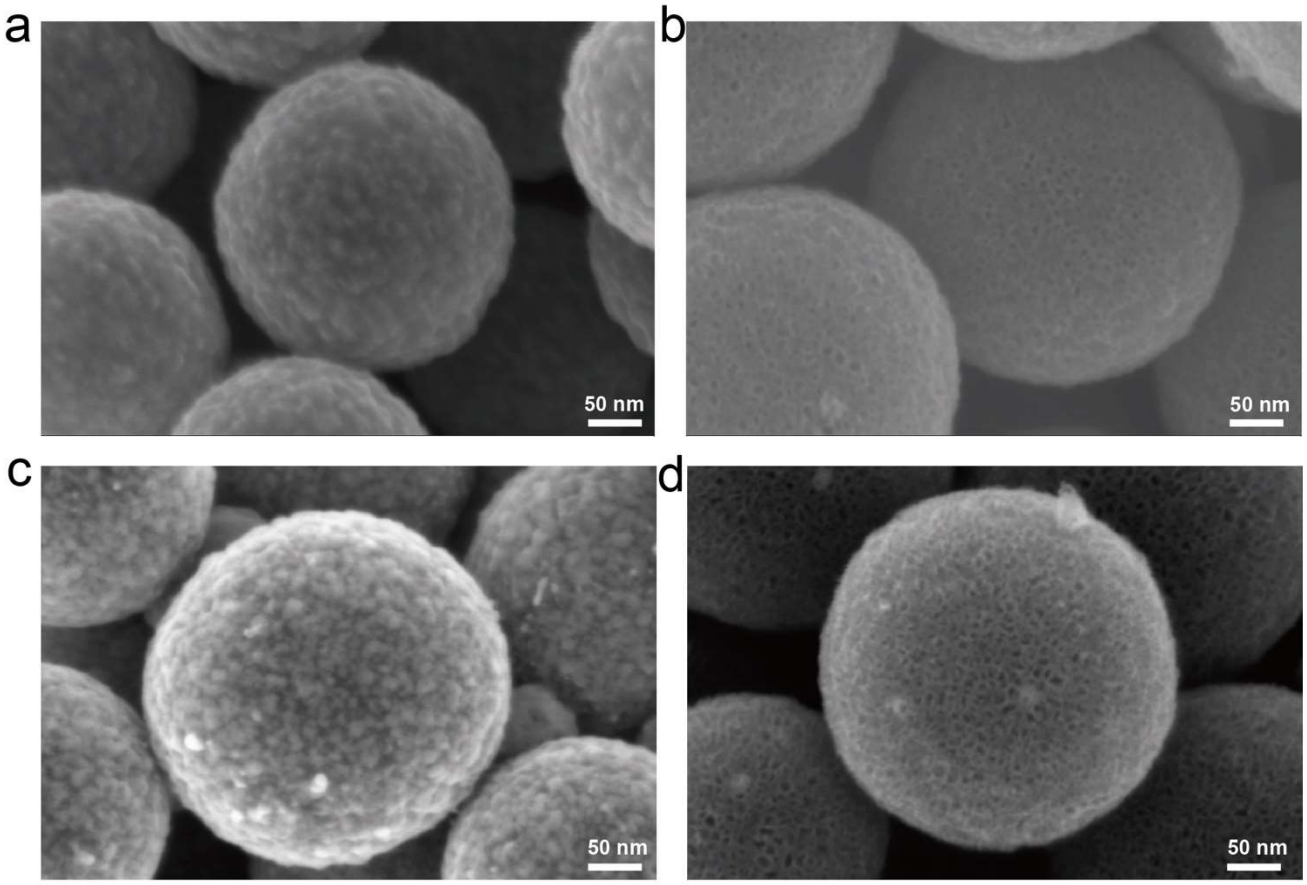

Supplementary Fig. S1| SEM characterization of MCHS. SEM images of **a** CS, **b** MCHS, **c** CuRu/CS and **d** CuRu/MCHS.

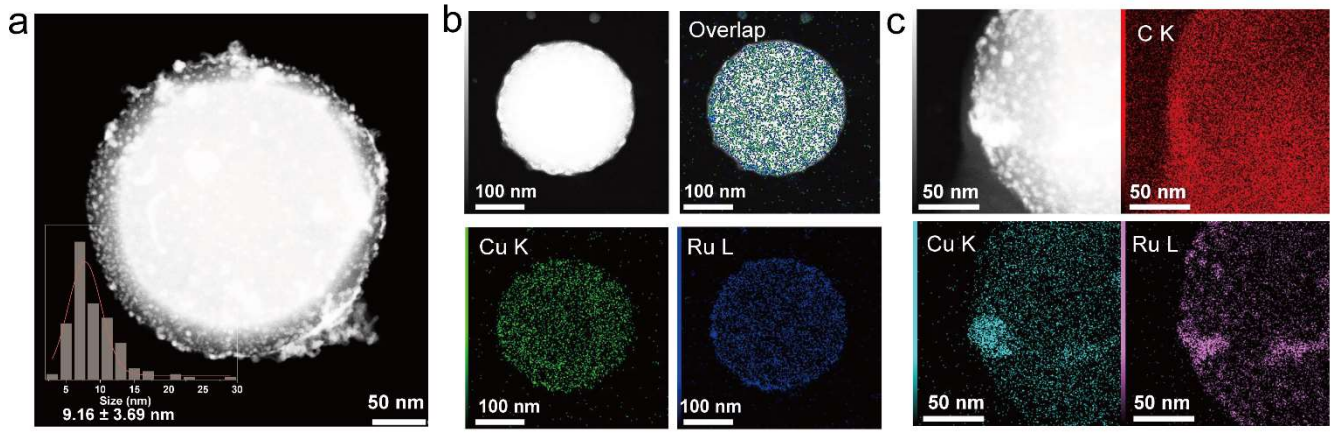

Supplementary Fig. S2| HAADF-STEM and EDS mapping of CuRu/CS. a, HAADF-STEM characterization and particle sizes distribution of CuRu/CS. **b**, EDS mapping profile of a single CuRu/CS. **c**, EDS mapping profile of localized enlarged area of CuRu/CS.

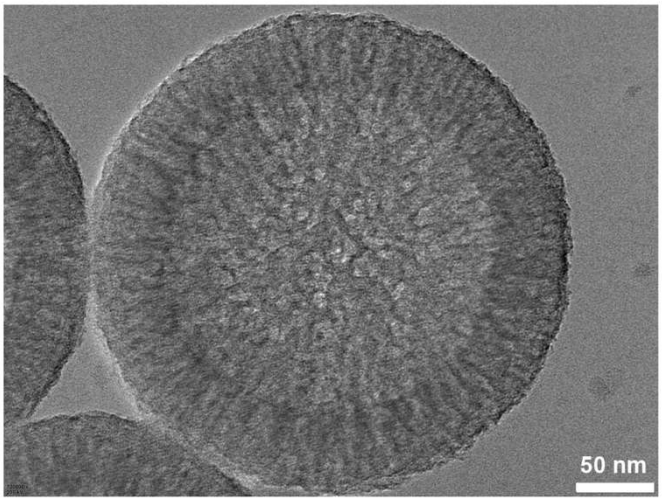

Supplementary Fig. S3| TEM characterization of MCHS.

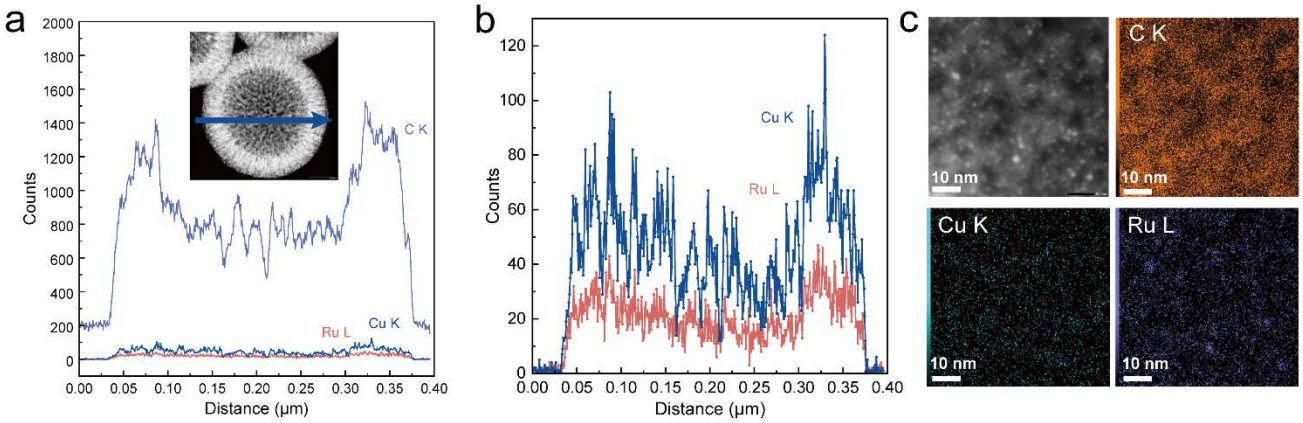

Supplementary Fig. S4| EDS mapping across a single CuRu/MCHS. a, EDS line-scan profiles of C, Cu, and Ru elements and **b** partial enlarged view of Cu and Ru elements. **c**, EDS mapping profile of the cavity region of CuRu/MCHS.

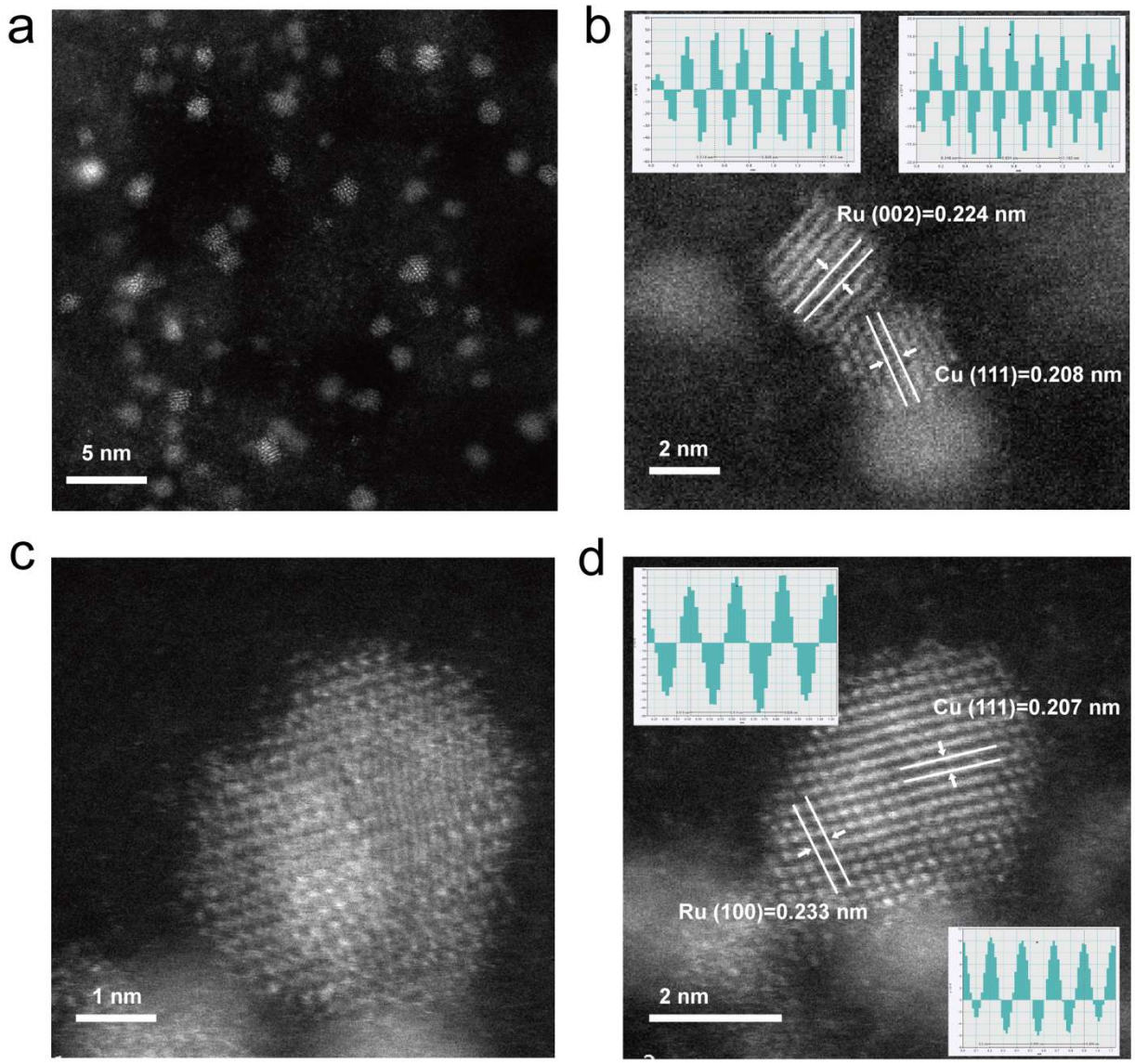

Supplementary Fig. S5| AC HAADF-STEM characterization of CuRu/MCHS. a, AC HAADF-STEM image of the cavity region of CuRu/MCHS. **b-d**, AC HAADF-STEM image of individual nanoclusters in CuRu/MCHS with calculated interplanar distances.

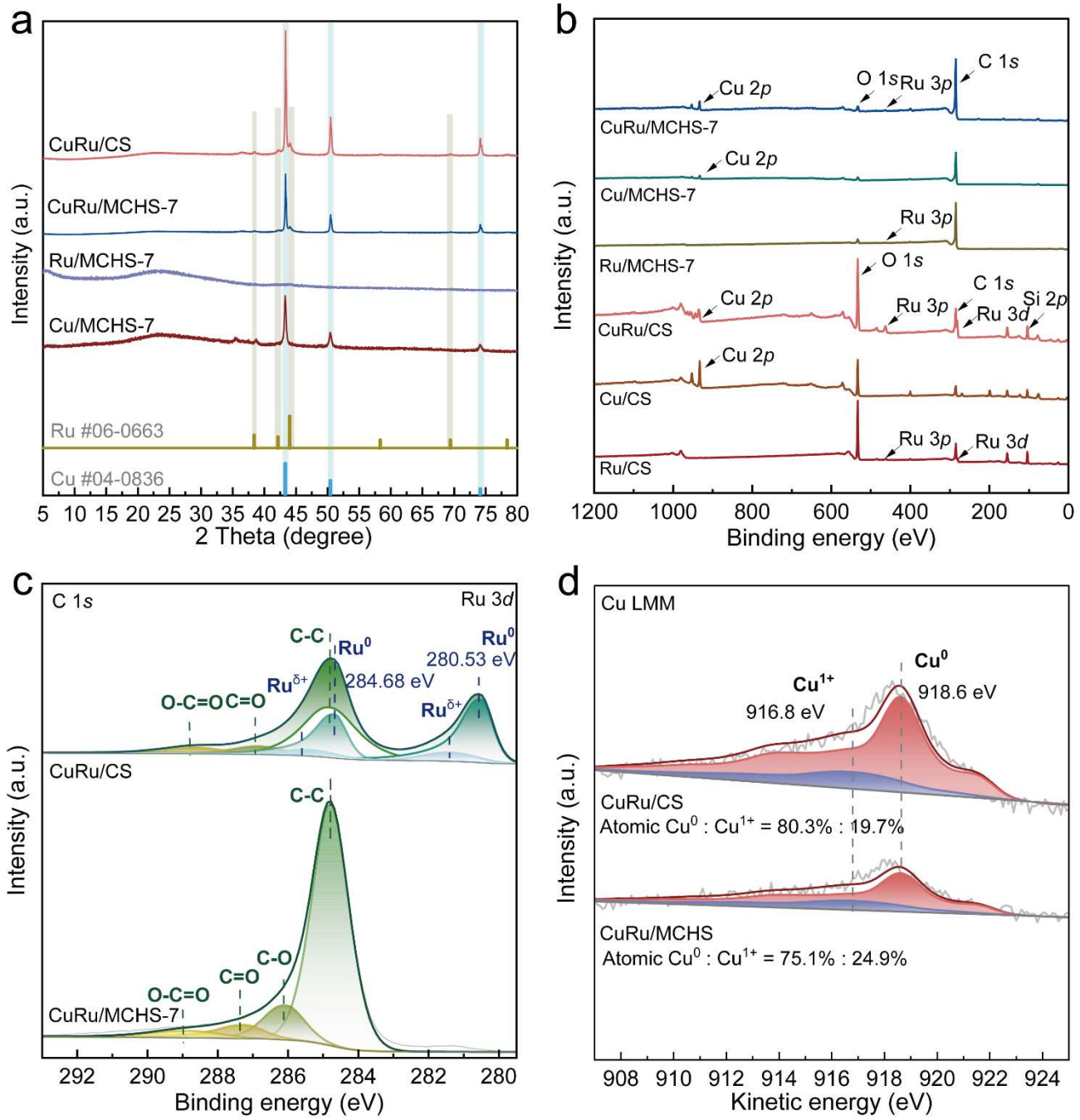

Supplementary Fig. S6| XRD and XPS characterization of samples. a, XRD patterns of CuRu/MCHS, CuRu/CS, Cu/MCHS, Ru/MCHS. **b**, Wide scanning survey spectrum of CuRu/MCHS, Cu/MCHS, Ru/MCHS, CuRu/CS, Cu/CS and Ru/CS. **c**, The XPS spectra and fit of C 1*s* of CuRu/MCHS. **d**, Cu LMM spectra of CuRu/MCHS and CuRu/CS. The a.u. stands for arbitrary units.

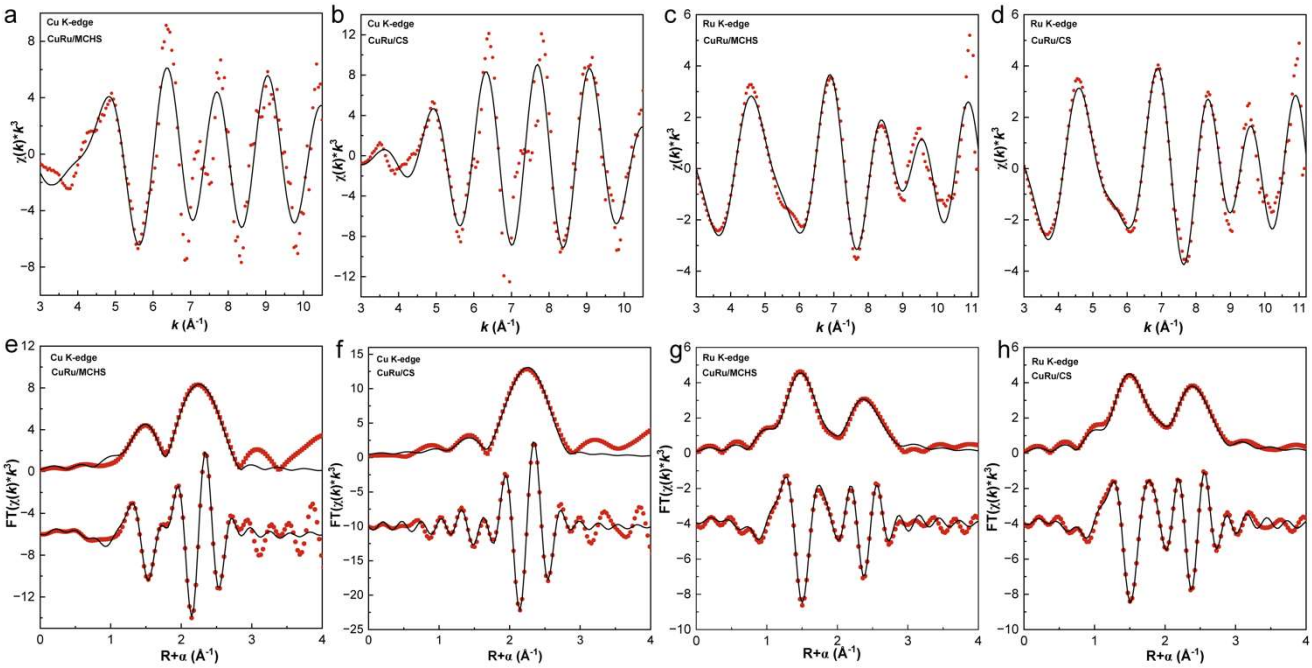

Supplementary Fig. S7| XAS spectra of Cu *K*-edge of CuRu/MCHS and CuRu/CS. Cu K-edge EXAFS (point) and the curve fit (line) for **a** CuRu/MCHS and **b** CuRu/CS shown in k^3-weight *k*-space. Ru K-edge EXAFS (point) and the curve fit (line) for **c** CuRu/MCHS and **d** CuRu/CS shown in k^3-weight *k*-space. Cu K-edge EXAFS (point) and the curve fit (line) for **e** CuRu/MCHS and **f** CuRu/CS shown in R-space (FT magnitude and imaginary component). Ru K-edge EXAFS (point) and the curve fit (line) for **g** CuRu/MCHS and **h** CuRu/CS shown in R-space (FT magnitude and imaginary component). The data are k^3-weight and not phase-corrected.

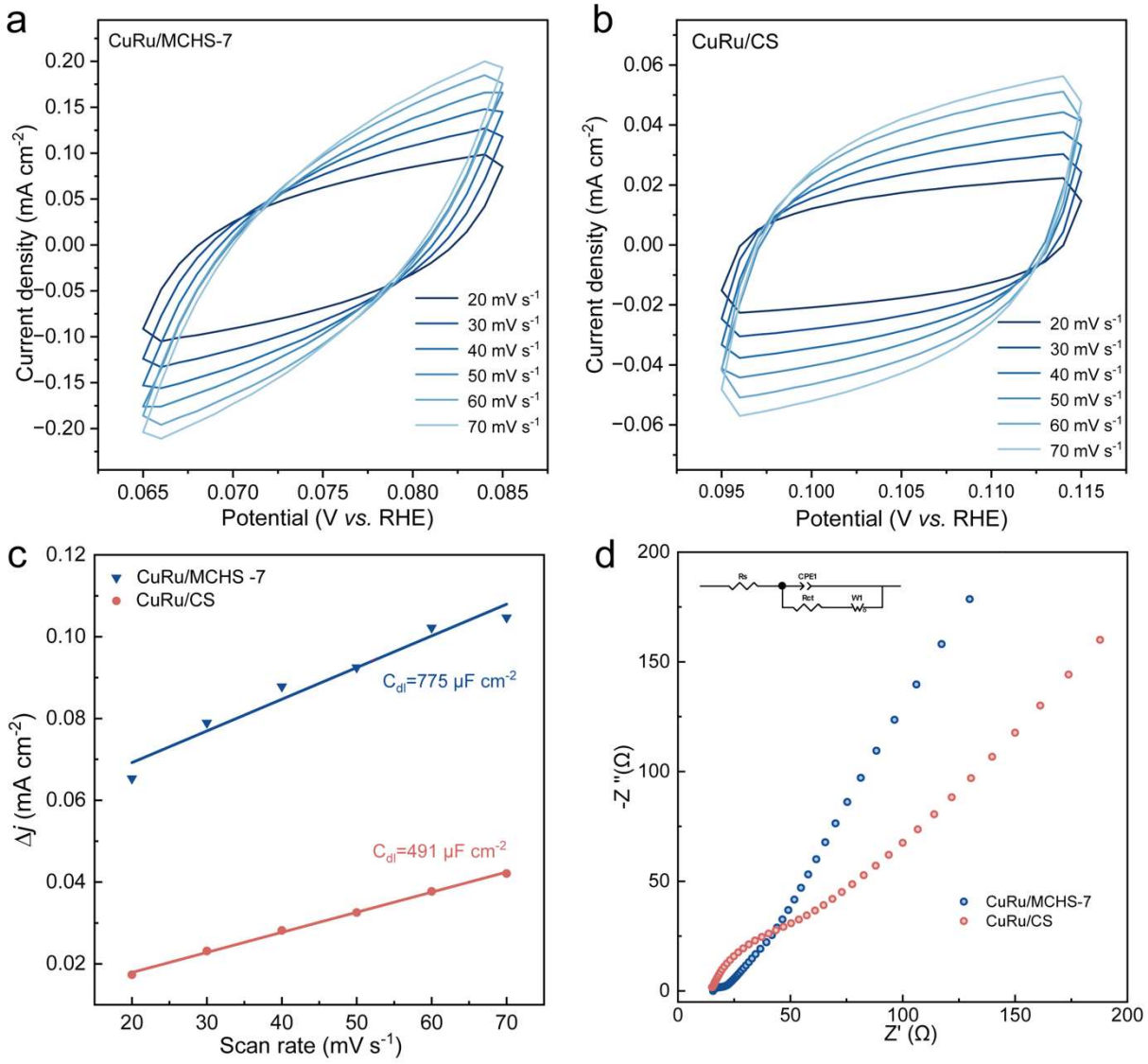

Supplementary Fig. S8| The electrochemical measurements on CuRu/MCHS and CuRu/CS. Cyclic voltammogram curves of **a** CuRu/MCHS and **b** CuRu/CS. **c**, *C*dl of corresponding electrocatalysts. **d**, The electrochemical impedance spectra of CuRu/MCHS and CuRu/CS cathodes from 1 M Hz to 0.1 Hz.

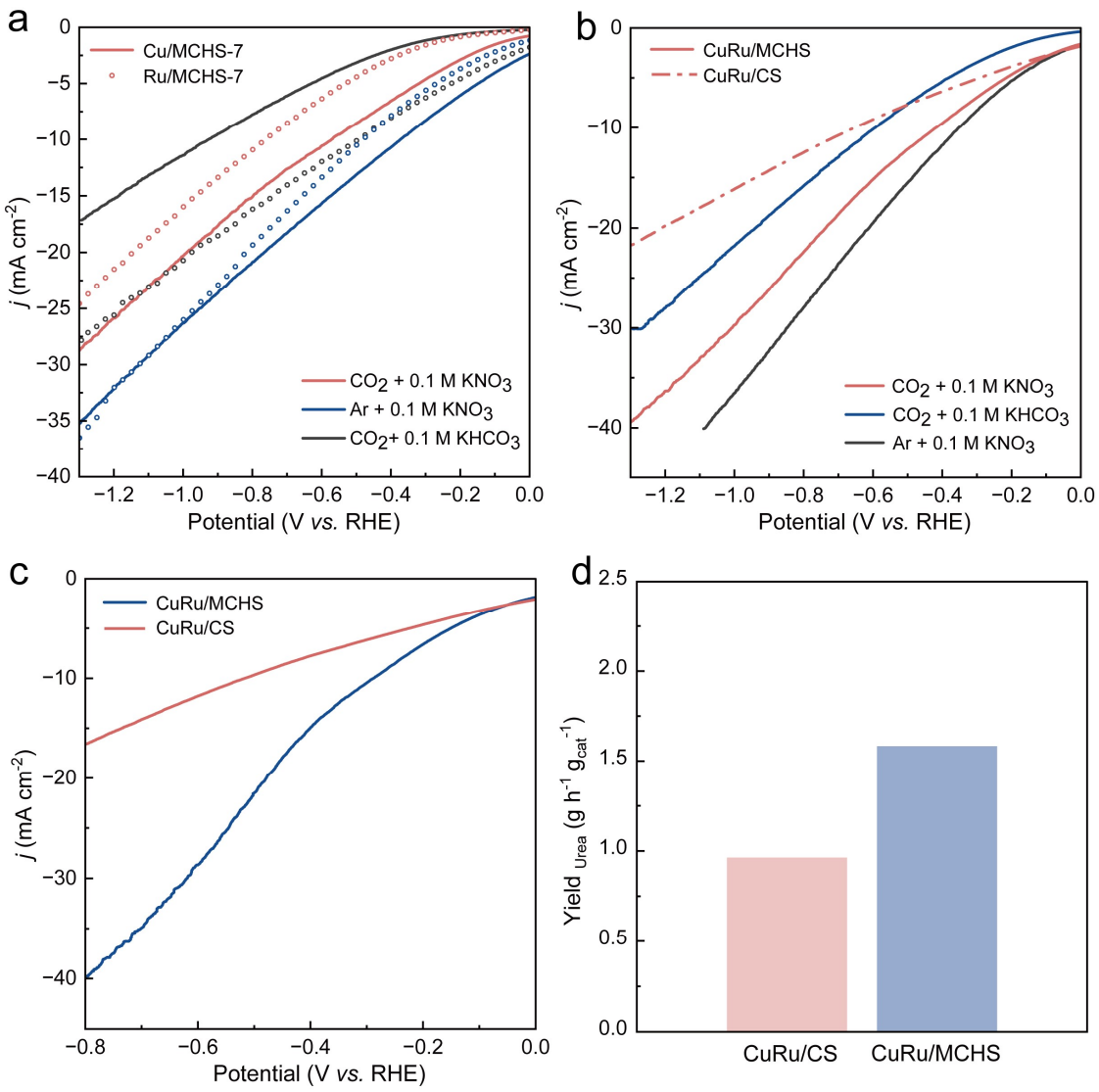

Supplementary Fig. S9| LSV curves of Cu/MCHS, Ru/MCHS, CuRu/CS and CuRu/MCHS at H-cell. a, LSV curves for a Cu/MCHS and Ru/MCHS without *iR* correction. **b**, LSV curves without *iR* correction for CuRu/MCHS and CuRu/CS in the mixture of 0.1 M KNO_3 under CO_2 flow in reference with that in 0.1 M KNO_3 + Ar and 0.1 M $KHCO_3$ + CO_2. The catalyst loading is 0.2 mg cm^{-2}. **c**, The *i*R-corrected LSV curves for CuRu/MCHS and CuRu/CS in the mixture of 0.1 M KNO_3 under CO_2 flow. The solution resistance (*R*s) values of CuRu/MCHS and CuRu/CS were 15.20 Ω and 15.96 Ω, respectively. 85% *i*R compensation was applied. **d**, Urea yield rate of CuRu/MCHS and CuRu/CS in H-cell at 20 mA cm^{-2}. At the same current density of 20 mA cm^{-2}, the urea production rates of CuRu/CS and CuRu/MCHS were 0.964 g h^{-1} g_{cat}^{-1} and 1.583 g h^{-1} g_{cat}^{-1}, respectively.

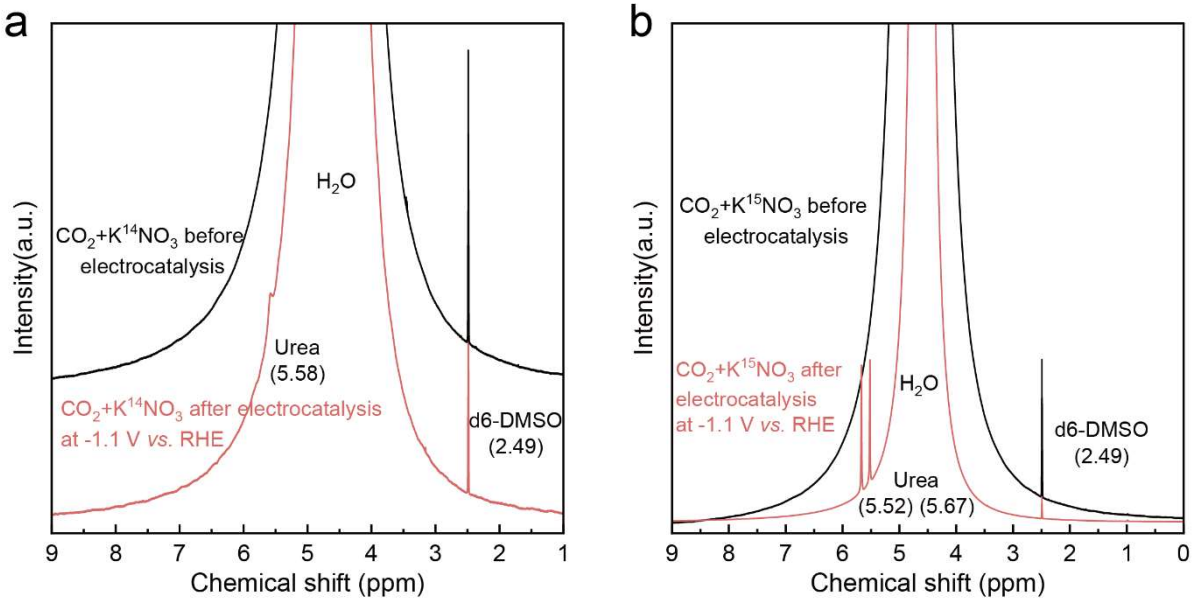

Supplementary Fig. S10| ^{1}H NMR measurements of liquid products. a, The curves the liquid product with CuRu/MCHS as electrocatalyst in 0.1 M KNO_3 as electrolyte (30 mL) at the potentials of –1.1 V (vs. RHE). **b**, The curves of the liquid product with CuRu/MCHS as electrocatalyst and 0.1 M $K^{15}NO_3$ as electrolyte (10 mL) at the potentials of –1.1 V (vs. RHE). The a.u. stands for arbitrary units.

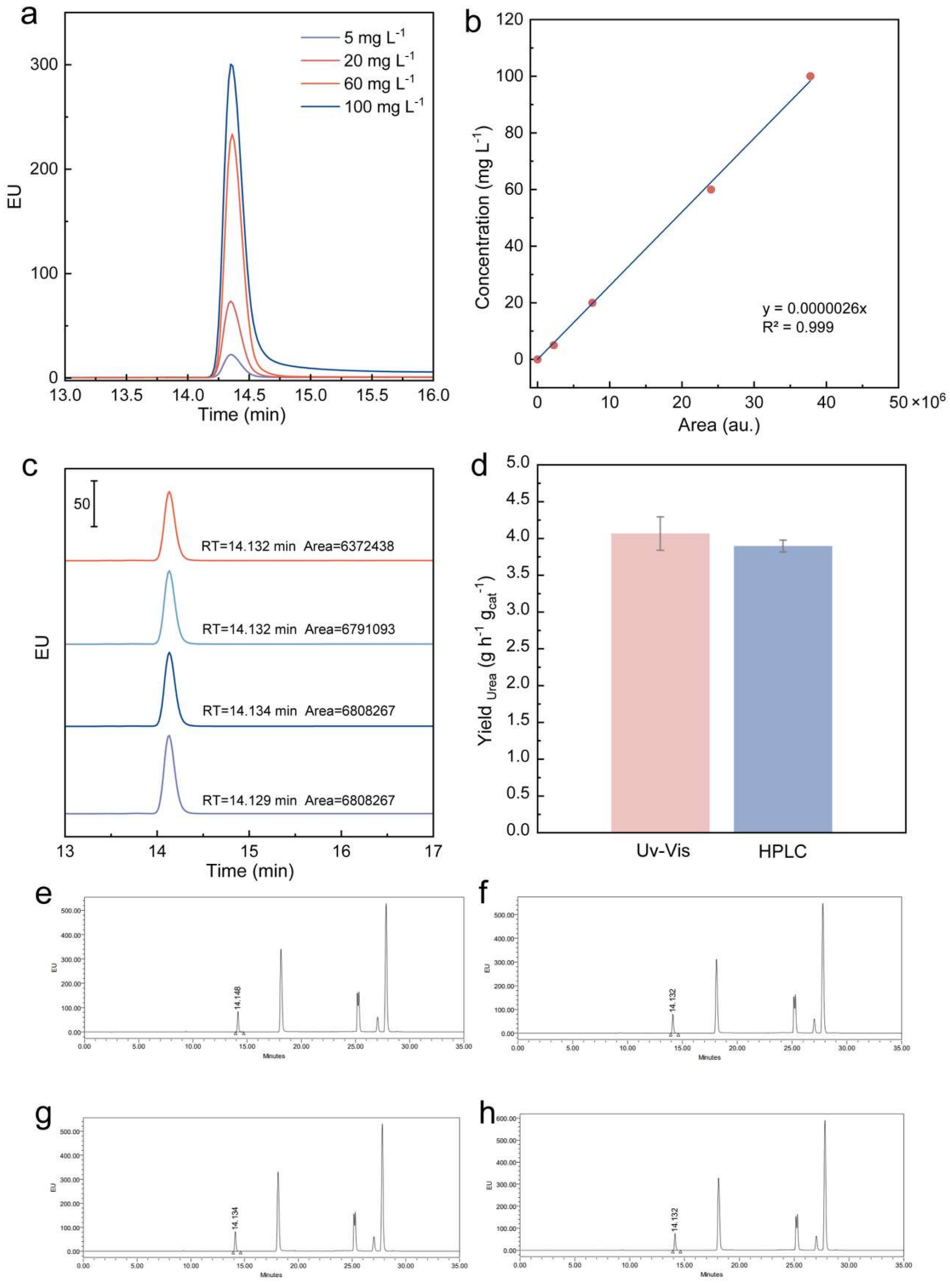

Supplementary Fig. S11| HPLC measurements of urea products. a, HPLC spectra of standard solutions containing different amounts of urea in 0.1 M KNO_3 solution. **b**, The calibration curve used to determine urea. **c**, HPLC spectra of urea in the liquid product after the reaction. **d**, The urea yield rate of CuRu/MCHS at –1.1 V (vs. RHE) detected by urease dissociation method and HPLC method. The data are presented as mean values ± s. d. (n = 4). **e-h**, The original HPLC spectra corresponding to the data.

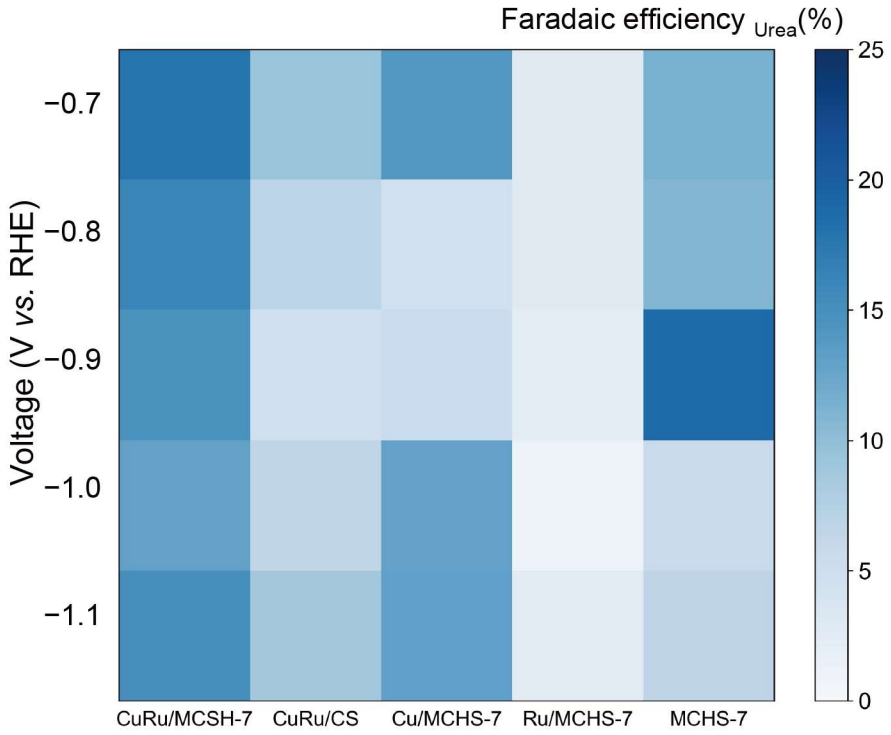

Supplementary Fig. S12| FE of urea performance comparison between electrocatalysts at various potential.

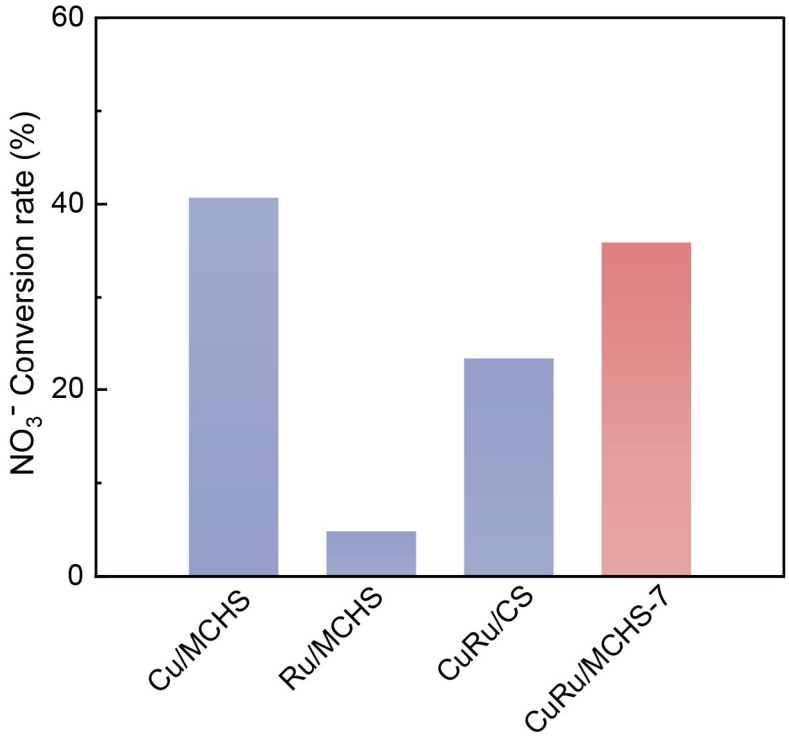

Supplementary Fig. S13| NO_3^- conversion rate of electrocatalytic CO_2 and NO_3^- co-reduction by Cu/MCHS, Ru/MCHS, CuRu/CS and CuRu/MCHS.

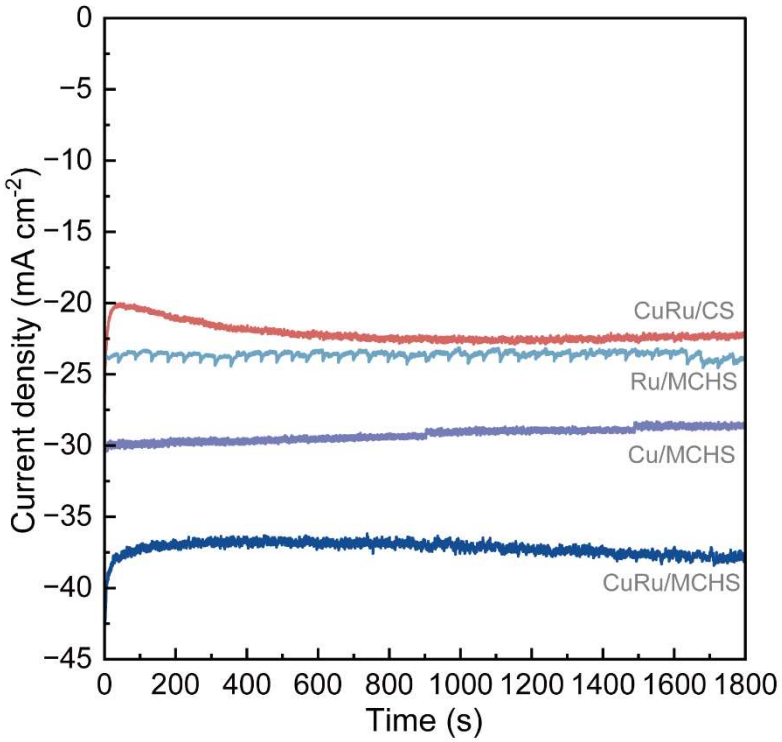

Supplementary Fig. S14| Performance of electrocatalytic CO_2 and NO_3^- co-reduction by samples in H-cell. I-t curves for electrocatalytic urea synthesis at –1.1 V vs. RHE on CuRu/MCHS, Cu/MCHS, Ru/MCHS, CuRu/CS.

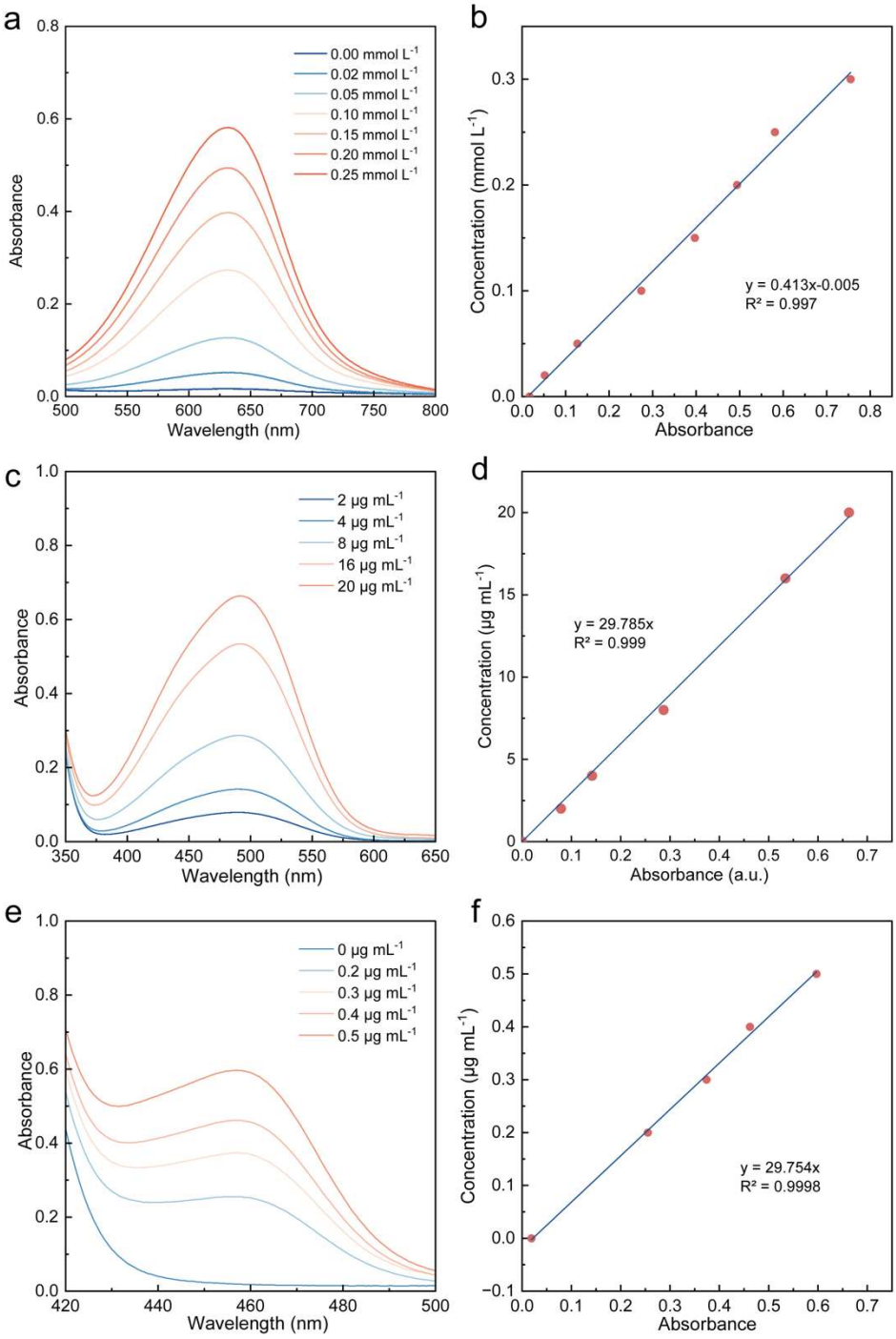

Supplementary Fig. S15| UV-vis measurements of the concentrations of NH_4^+, NO_2^-, N_2H_4. a, UV-vis spectra of various NH_4^+ standard solution. **b**, The calibration curve for quantification of NH_4^+ indicates good linear relation of absorbance with NH_4^+ concentration. **c**, UV-vis spectra of various NO_2^- standard solution. **d**, The calibration curve for quantification of NO_2^- indicates good linear relation of absorbance with NO_2^- concentration. **e**, UV-vis spectra of various N_2H_4 standard solution. **f**, The calibration curve for quantification of N_2H_4 indicates good linear relation of absorbance with N_2H_4 concentration.

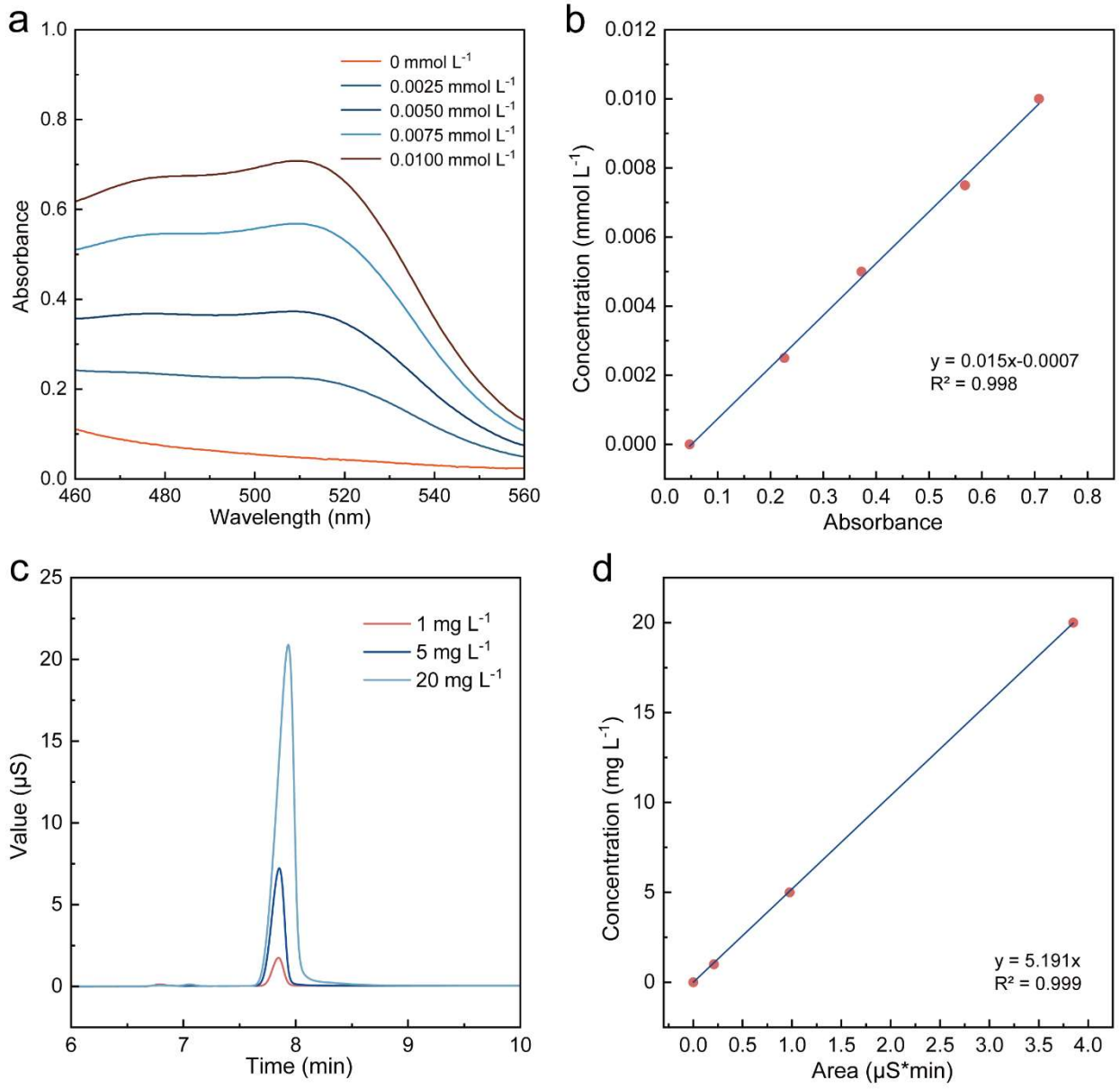

Supplementary Fig. S16| Measurements of the concentrations of NH_2OH and HCOOH. a, UV-vis spectra of various NH_2OH standard solution in 0.1 M KNO_3. **b**, The calibration curve for quantification of NH_2OH indicates good linear relation of absorbance with NH_2OH concentration. **c**, IC spectra of various HCOOH standard solution in 0.1 M KNO_3. **d**, The calibration curve for HCOOH quantification indicates good linear relationship with concentration**.**

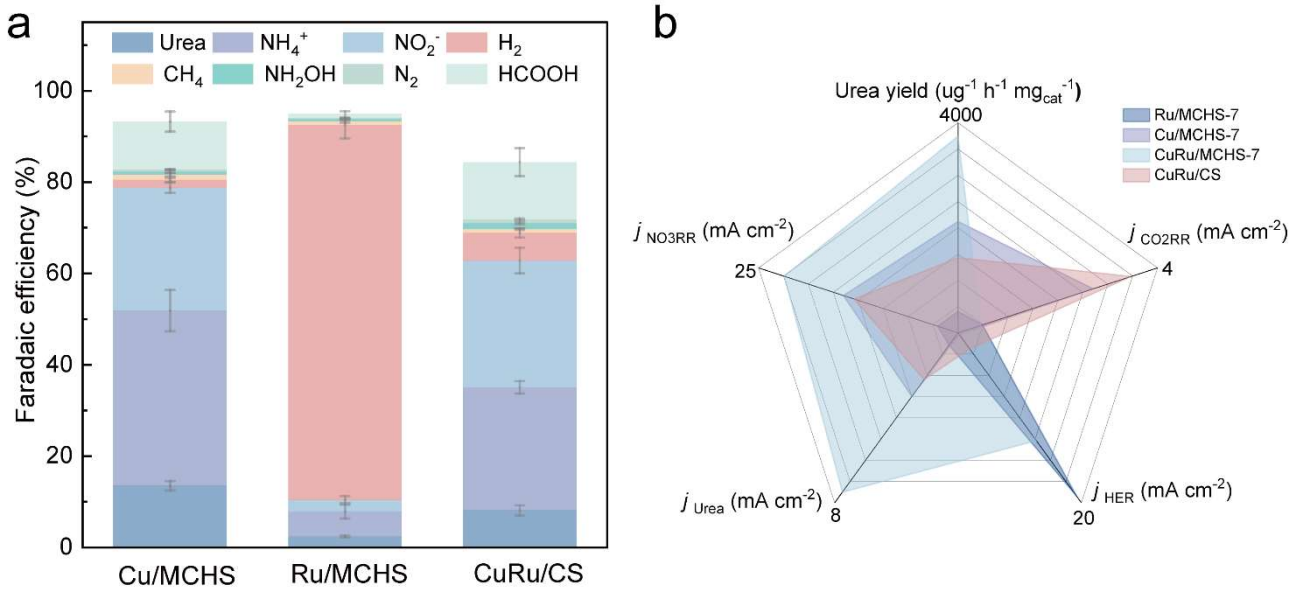

Supplementary Fig. S17| Performance of electrosynthesis of urea. a, FEs of CH_4, H_2, NO_2^-, NH_4^+, NH_2OH, N_2, HCOOH and urea of Cu/MCHS, Ru/MCHS and CuRu/CS as electrocatalyst at the potential of –1.1 V (vs. RHE). CO and N_2H_4 by-products were not detected under any conditions The data are presented as mean values ± s.d. (n = 3). **b**, Comparison of various properties of CuRu/MCHS, CuRu/CS, Cu/MCHS and Ru/MCHS catalysts.

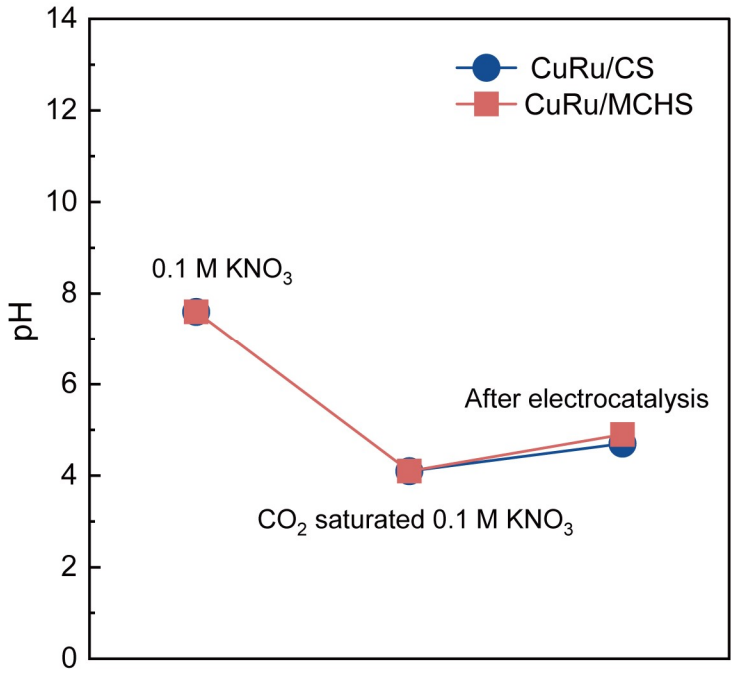

Supplementary Fig. S18| The pH variation plots of CuRu/MCHS and CuRu/CS before and after the electrocatalysis.

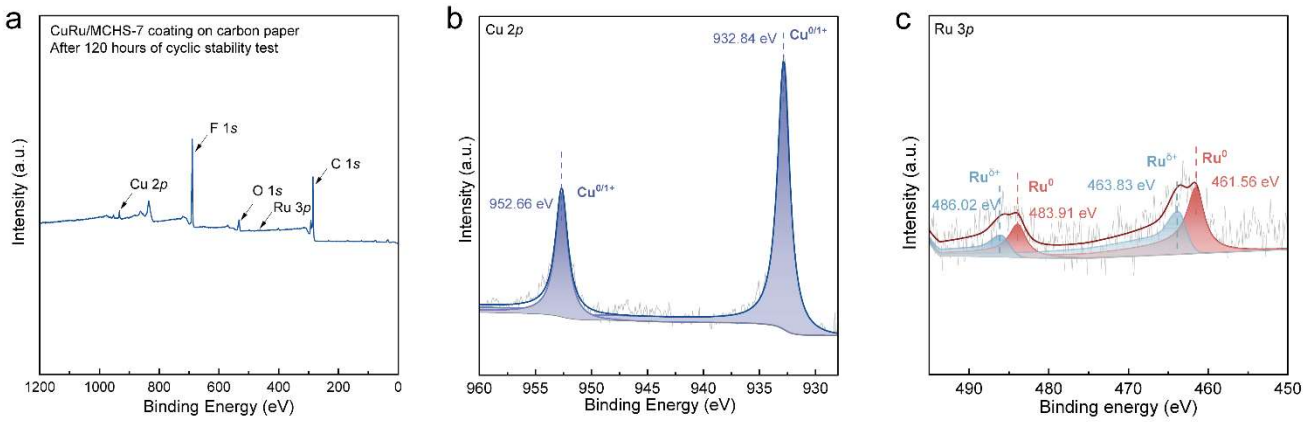

Supplementary Fig. S19| XPS characterization of CuRu/MCHS after 125 hours cyclic stability test. **a**, Wide scanning survey spectrum of working electrode with CuRu/MCHS electrocatalyst. The XPS spectra and fit of **b** Cu 2*p* and **c** Ru 3*p*. The a.u. stands for arbitrary units.

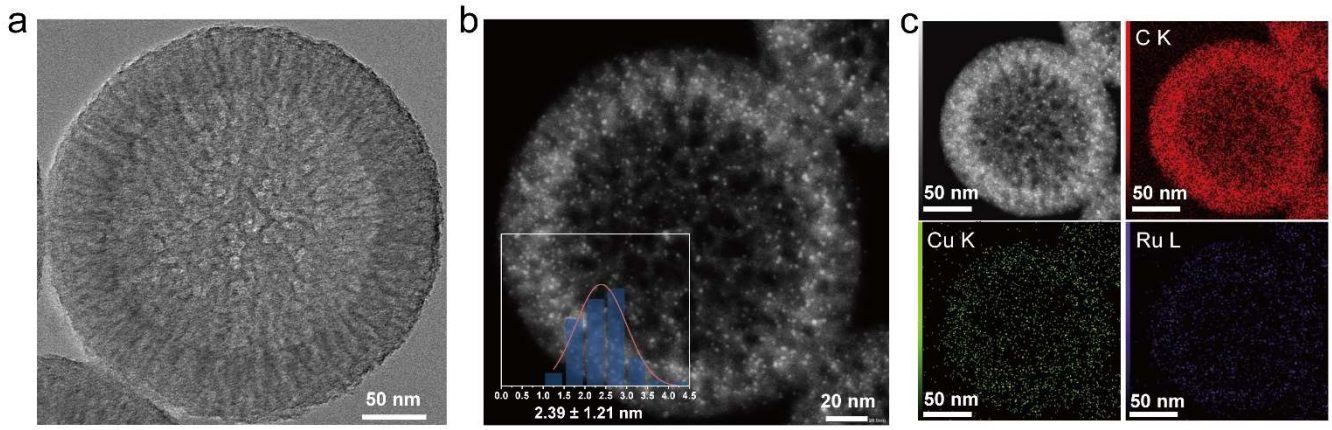

Supplementary Fig. S20| Structural information of CuRu/MCHS after electrocatalysis. a, HR-TEM image of CuRu/MCHS after electrocatalysis. **b**, HAADF-STEM characterization and particle size distribution of CuRu/MCHS after stability test. **c**, EDS mapping profile of CuRu/MCHS after stability test.

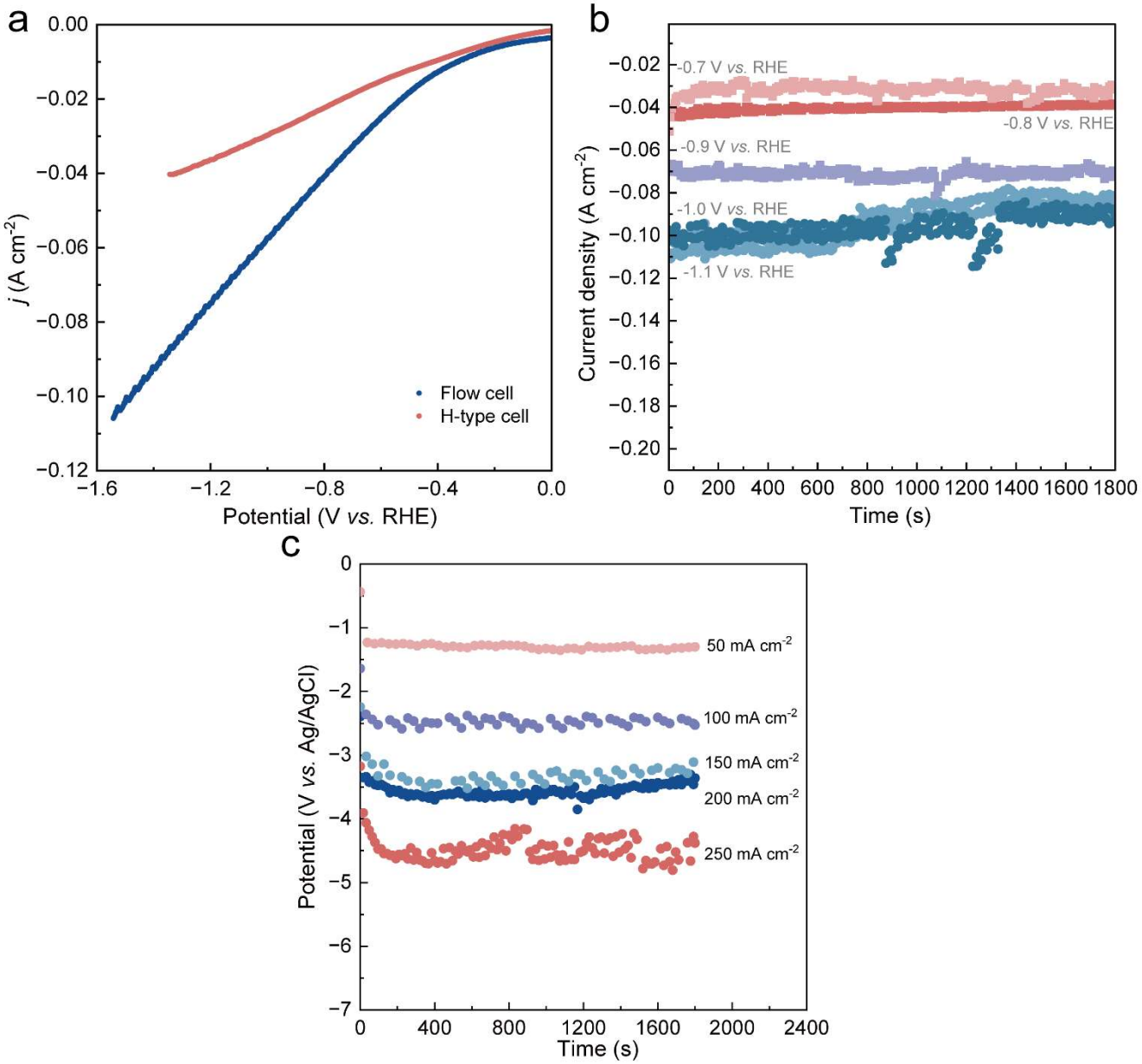

Supplementary Fig. S21| Performance of electrocatalytic CO_2 and NO_3^- co-reduction by CuRu/MCHS in flow cell. a, LSV curves for CuRu/MCHS at the H-cell and flow cell with 0.1 M KNO_3 + CO_2 as electrolyte and without *iR* correction. The catalyst loading is 0.2 mg cm^{-2}. **b**, I-t curves for electrocatalytic urea synthesis at various applied potential on CuRu/MCHS. **c**, Chronopotentiometry (CP) measurement for urea synthesis at various current density on CuRu/MCHS.

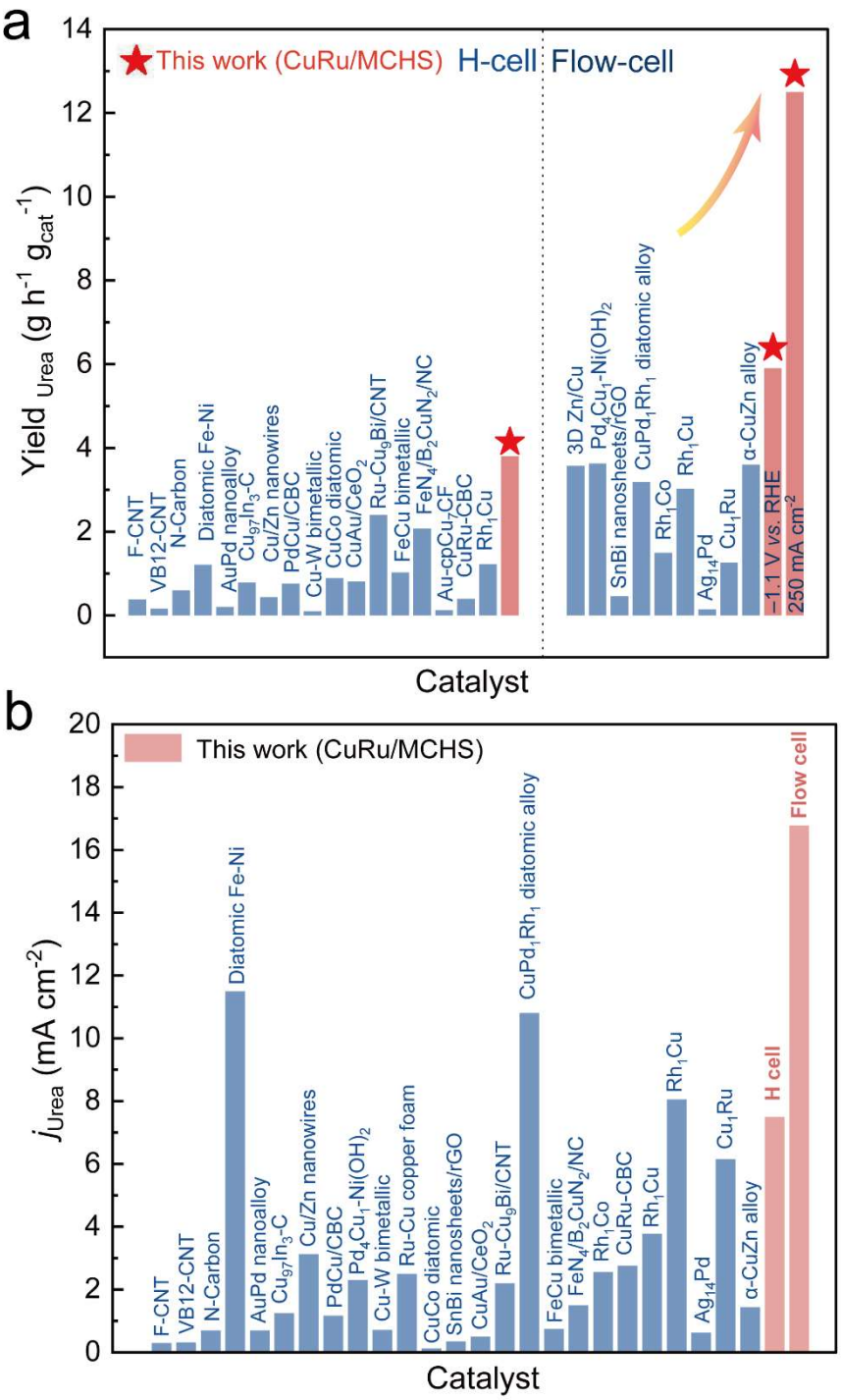

Supplementary Fig. S22| Comparison of a urea formation rate and b j_{Urea} between CuRu/MCHS and other bimetallic catalysts reported in the literatures. Corresponding values are tabulated in the Table S8.

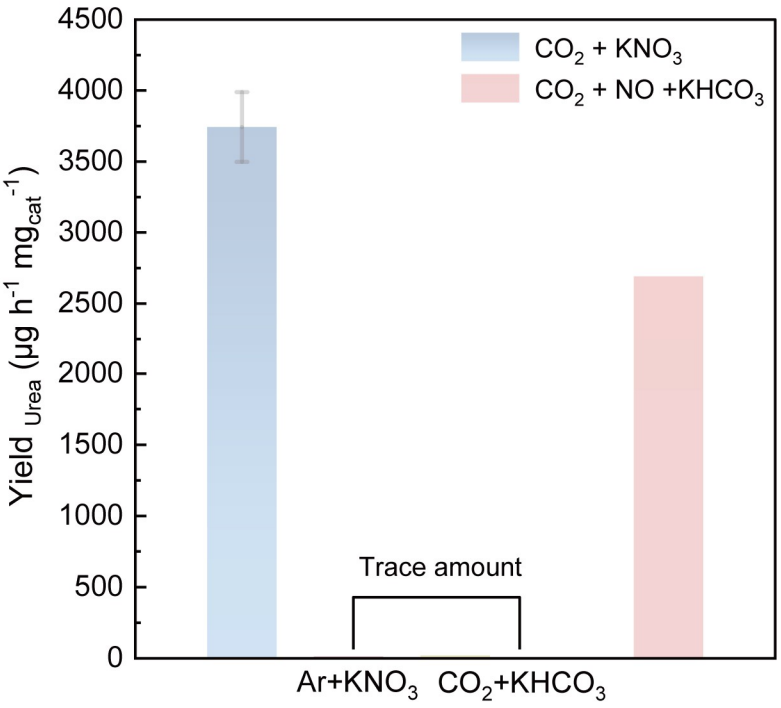

Supplementary Fig. S23| Urea yield rates of CuRu/MCHS with various feedstocks at –1.1 V (vs. RHE). The data are presented as mean values ± s.d. (n ≥ 3).

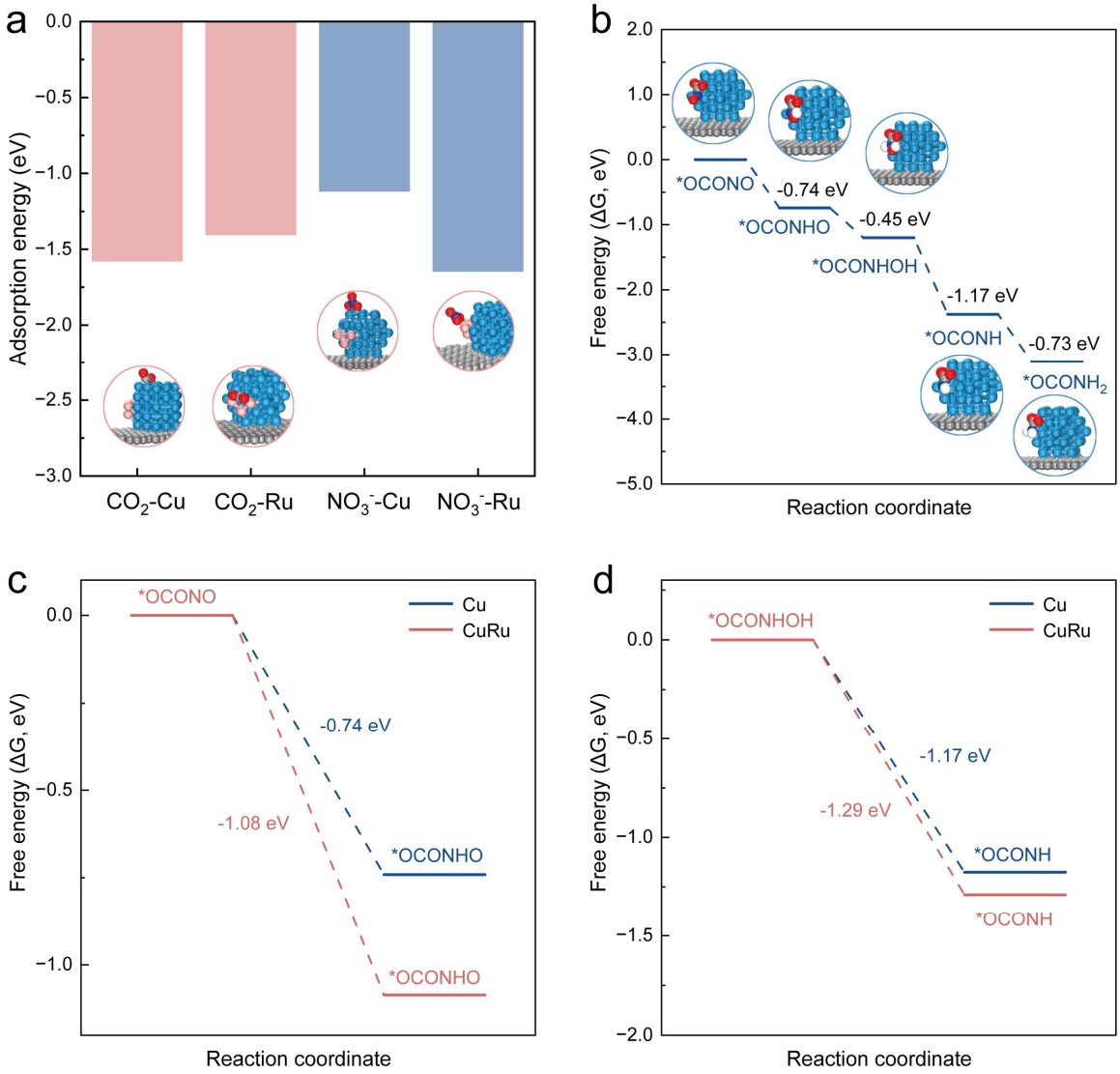

Supplementary Fig. S24| DFT calculations of urea production on CuRu and Cu surface. a, Comparison of CO_2 and NO_3^- adsorption energies on Cu site and Ru site of the CuRu model. **b**, Energy profiles of each elementary step in C–N coupling toward urea synthesis on the Cu model and corresponding atomic configurations. The gray, blue, red, white, pink and turquoise balls represent C, N, O, H, Cu and Ru atoms, respectively. **c**, Energy profiles of *OCONO to *OCONHO step on the CuRu and Cu model.**d**, Energy profiles of *OCONHOH to *OCONH step on the CuRu and Cu model.

l.

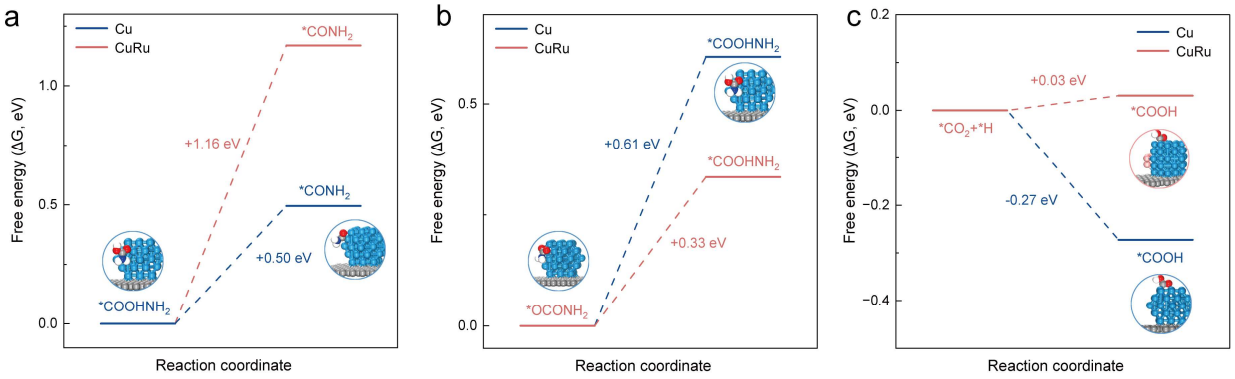

Supplementary Fig. S25| DFT calculations of CO_2RR and C–N coupling on CuRu and Cu surface. **a**, Energy profiles of *$COOHNH_2$ to *$CONH_2$ step on the CuRu and Cu model. **b**, Energy profiles of *$OCONH_2$ to *$COOHNH_2$ step on the CuRu and Cu model. **c**, Energy profiles of *CO_2 to *COOH step on the CuRu and Cu model. The gray, blue, red, white, pink and turquoise balls represent C, N, O, H, Cu and Ru atoms, respectively.

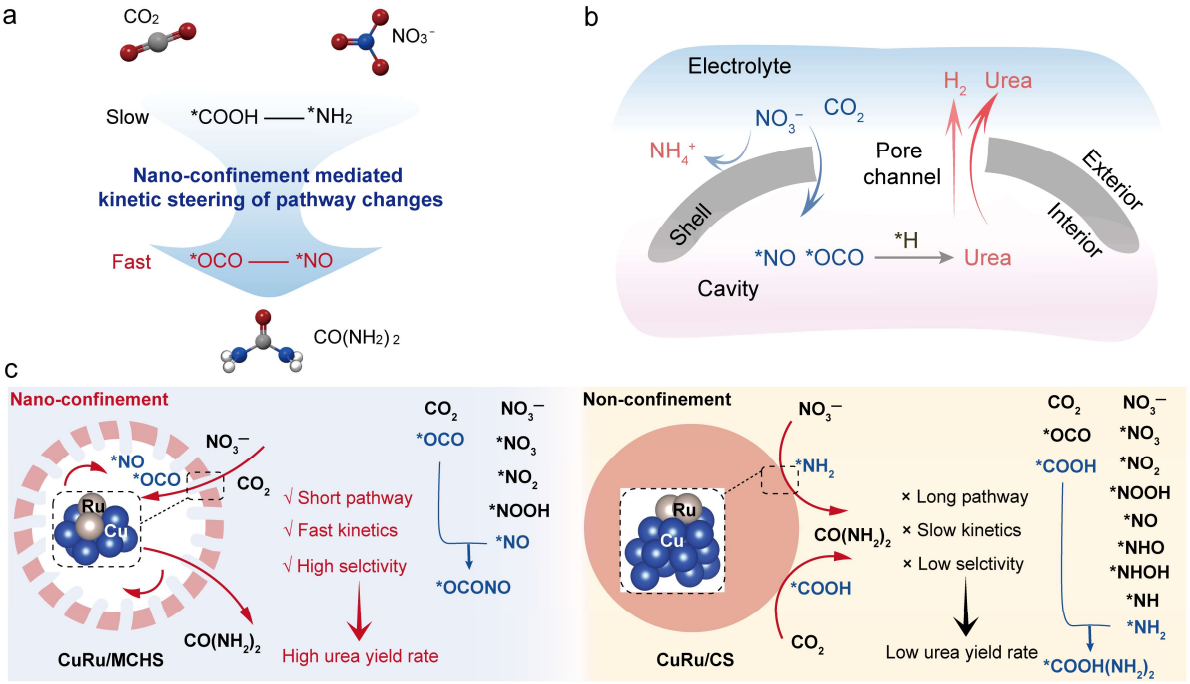

Supplementary Fig. S26| Schematic illustration of reaction pathway conversion in CuRu/MCHS and CuRu/CS. Conceptual diagram of the **a** reaction comparison and **b** pathway transition between nano-confined and non-confined catalysts. **c**, The diffusion and transformation of reactants and products within the cavities and pores of CuRu/MCHS.

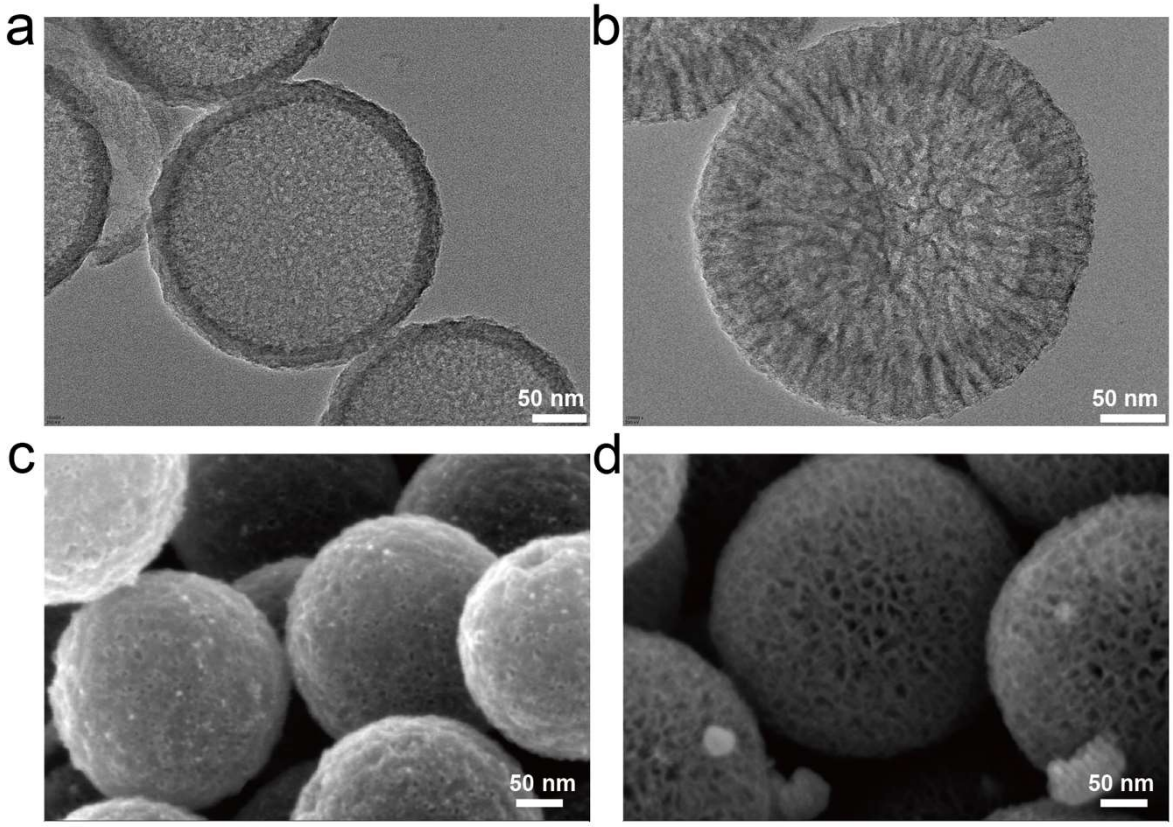

Supplementary Fig. S27| SEM and TEM characterization of MCHS-4, MCHS-11, CuRu/MCHS-4 and CuRu/MCHS-11. TEM images **a** MCHS-4 and **b** MCHS-11. SEM images **c** CuRu/MCHS-4 and **d** CuRu/MCHS-11.

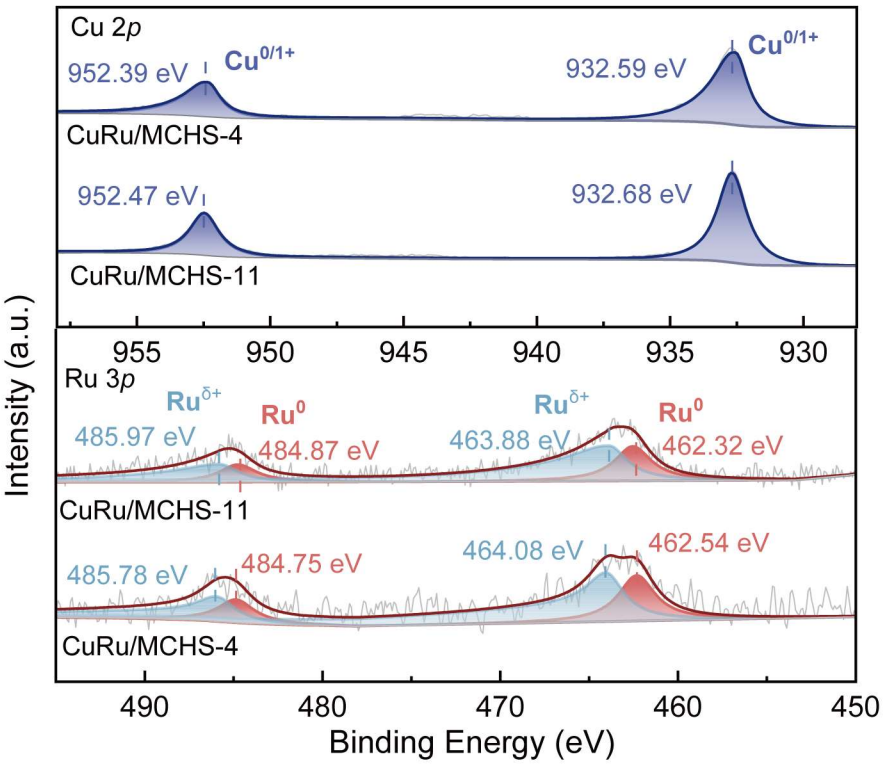

Supplementary Fig. S28| XPS characterization of CuRu/MCHS-4 and CuRu/MCHS-11. The XPS spectra and fit of Cu 2*p* (up) and Ru 3*p* (down) of CuRu/MCHS-4 and CuRu/MCHS-11. The a.u. stands for arbitrary units.

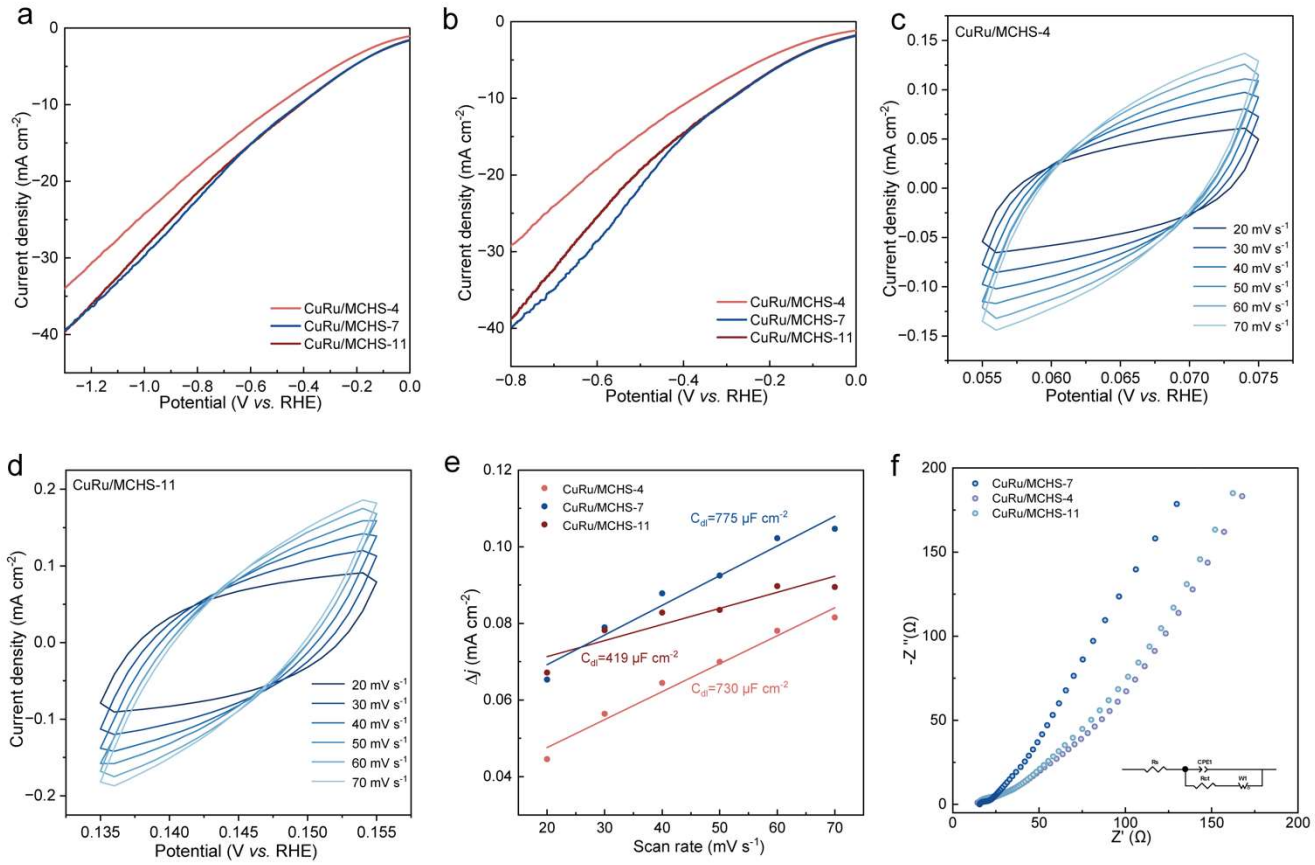

Supplementary Fig. S29| The electrochemical measurements on CuRu/MCHS-4 and CuRu/MCHS-11. a, LSV curves and **b** *i*R-corrected LSV curves of electrocatalytic CO_2 and NO_3^- co-reduction by CuRu/MCHS-4, CuRu/MCHS-7 and CuRu/MCHS-11. The *R*s values of CuRu/MCHS-4, CuRu/MCHS-7, and CuRu/MCHS-11 were 14.31 Ω, 15.20 Ω, and 14.39 Ω, respectively. 85% *i*R compensation was applied. Cyclic voltammogram curves of **c** CuRu/MCHS-4 and **d** CuRu/MCHS-11. **e**, *C*dl of corresponding electrocatalysts. **f**, The electrochemical impedance spectra in of CuRu/MCHS-4, CuRu/MCHS-7 and CuRu/MCHS-11 cathodes from 1 M Hz to 0.1 Hz.

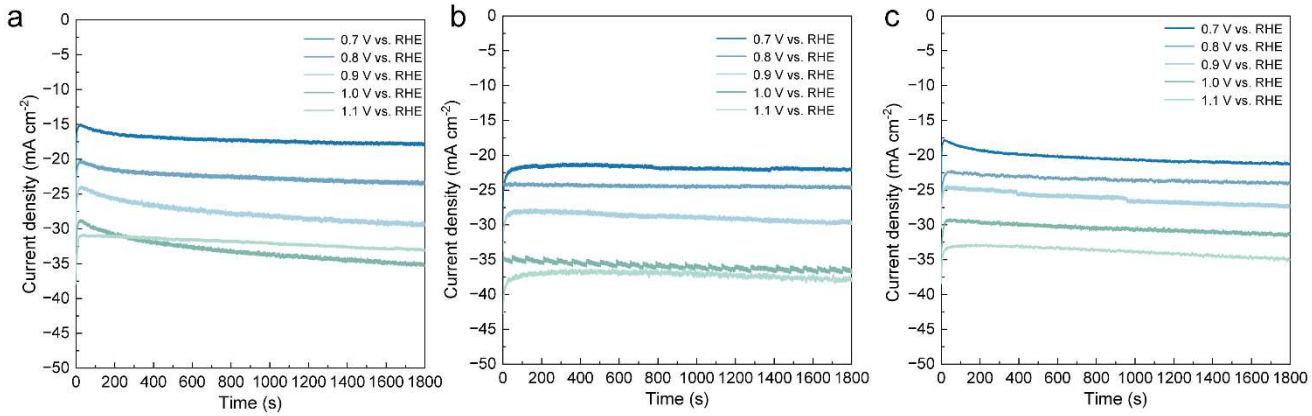

Supplementary Fig. S30| Performance of electrocatalytic CO_2 and NO_3^- co-reduction by samples at various potential in H-cell. I-t curves for electrocatalytic urea synthesis at various applied potential on **a** CuRu/MCHS-4, **b** CuRu/MCHS-7 and **c** CuRu/MCHS-11.

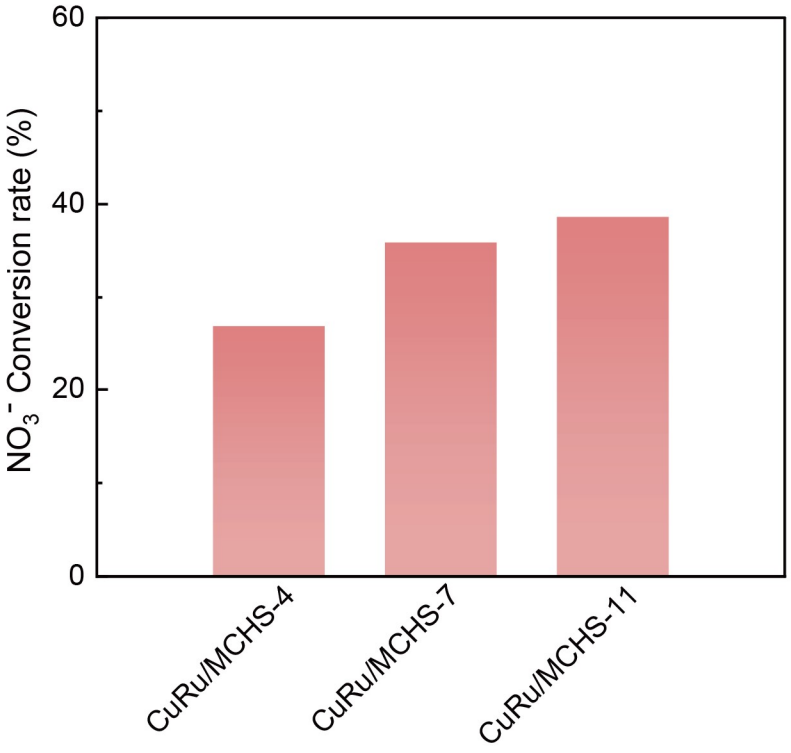

Supplementary Fig. S31| NO_3^- conversion rate of electrocatalytic CO_2 and NO_3^- co-reduction by CuRu/MCHS-4, CuRu/MCHS-7 and CuRu/MCHS-11.

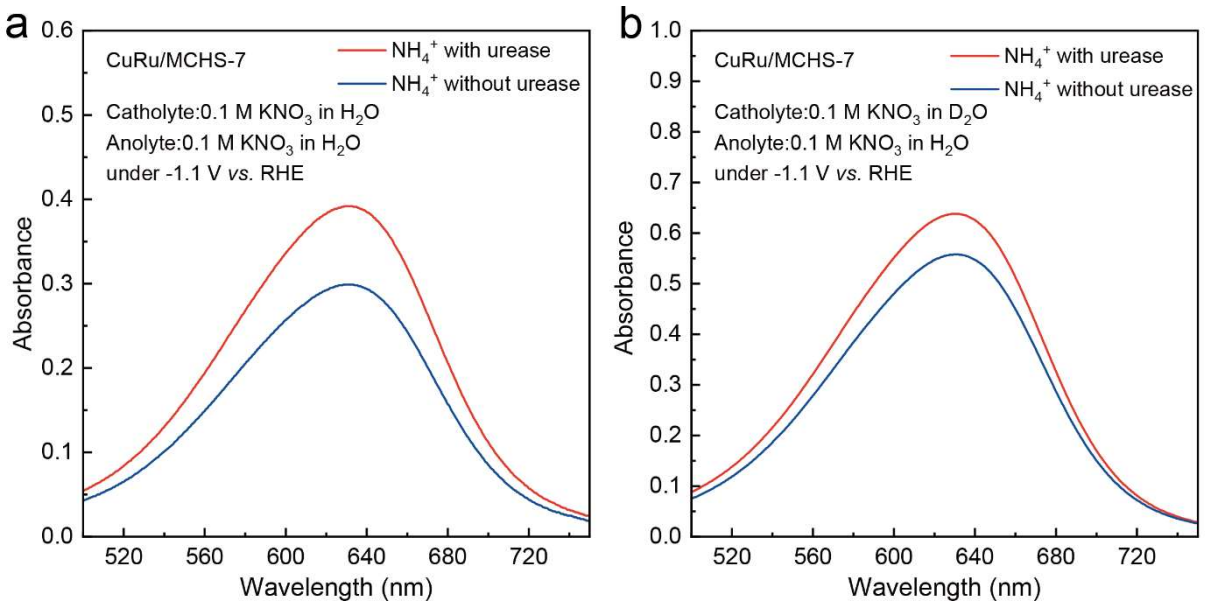

Supplementary Fig. S32| UV-vis measurements of products by CuRu/MCHS-7. a, UV-vis measurements of NH_4^+ to determine urea with urase with 0.1 M KNO_3 as anolyte and catholyte at the potentials of –1.1 V (vs. RHE). **b**, UV-vis measurements of NH_4^+ to determine urea with urase with 0.1 M KNO_3 (H_2O) as anolyte and 0.1 M KNO_3 (D_2O) as catholyte at the potentials of –1.1 V (vs. RHE).

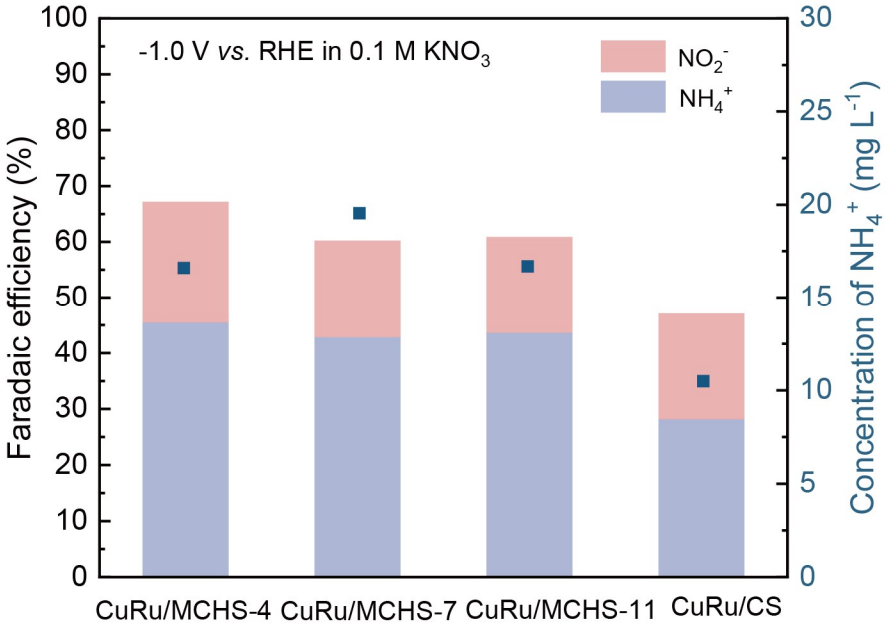

Supplementary Fig. S33| Performance of electrocatalytic NO_3^- reduction by samples. The FE and the concentration of NH_4^+ with samples as electrocatalysts.

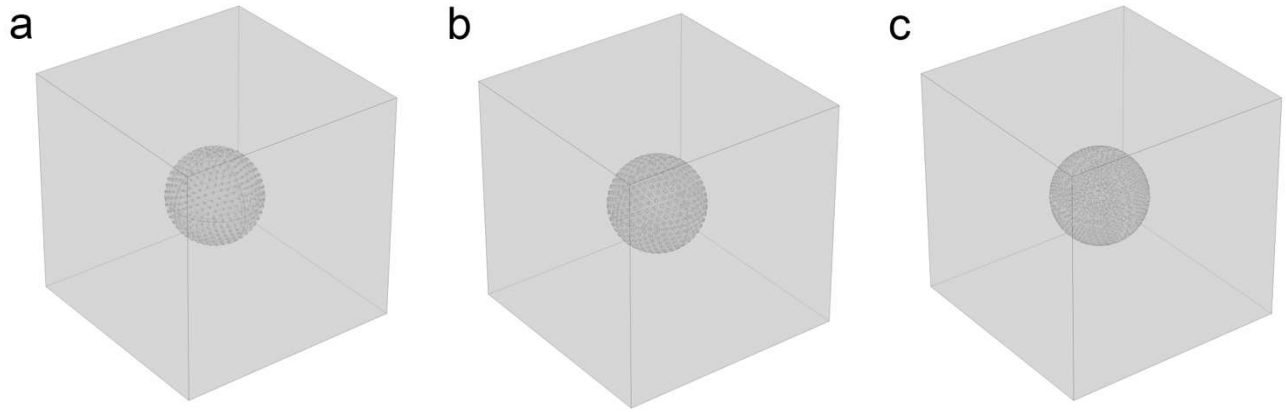

Supplementary Fig. S34| The initial models for FEM calculation. a, CuRu/MCHS-4, **b**, CuRu/MCHS-7 and **c**, CuRu/MCHS-11

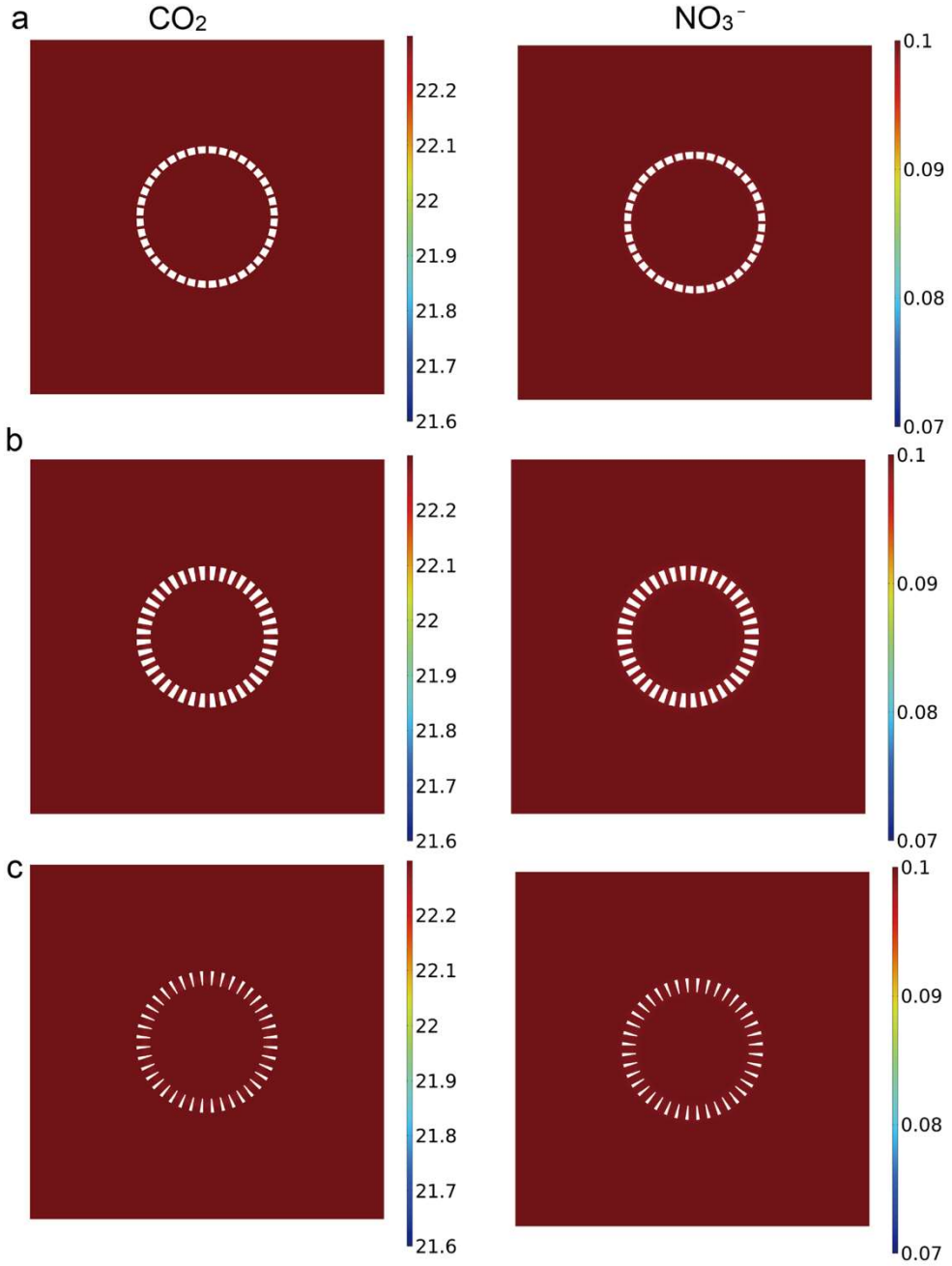

Supplementary Fig. S35| The initial concentration of CO_2 and NO_3^-. a, CuRu/MCHS-4, **b**, CuRu/MCHS-7 and **c**, CuRu/MCHS-11. Color scale, in mol L^{-1}.

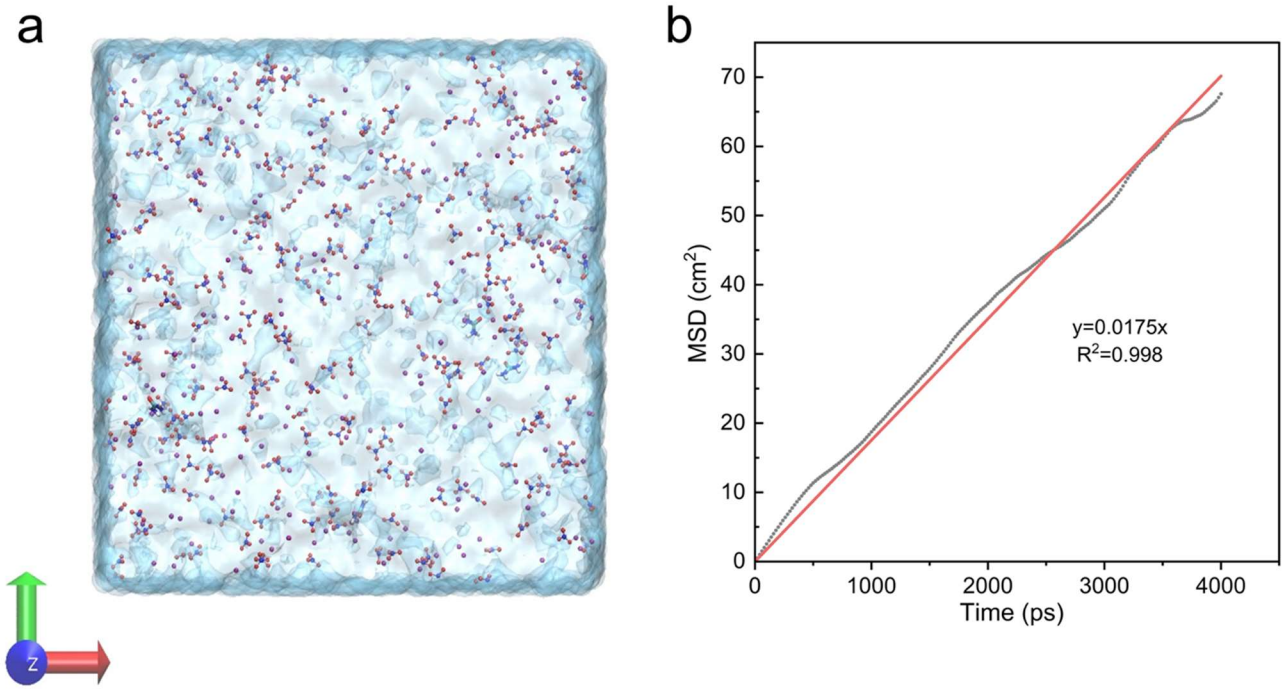

Supplementary Fig. S36| The self-diffusion coefficient of urea. a, The final equilibration snapshots for the dynamic diffusion process and the **b** corresponding MSD versus time plot in logarithmic scale for urea in KNO_3 aqueous solution at 298.15 K.

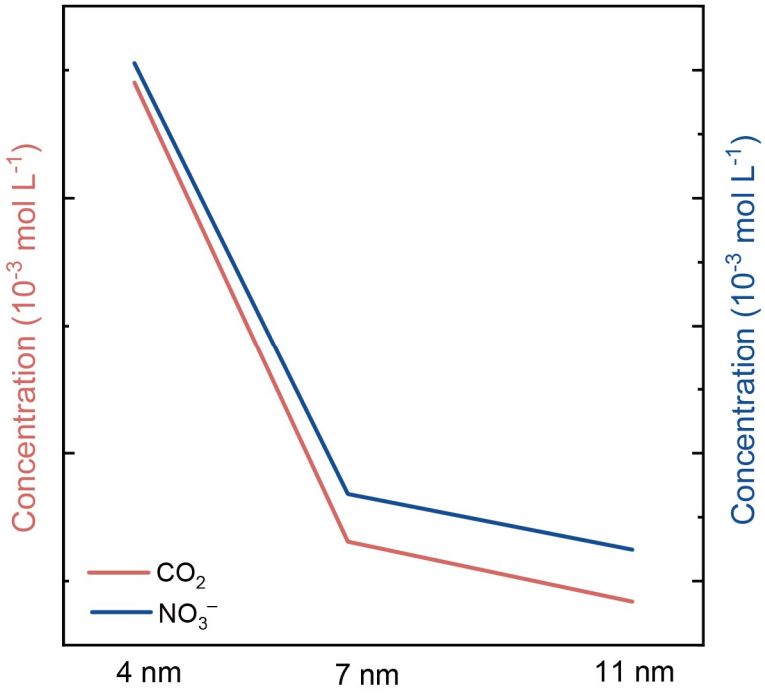

Supplementary Fig. S37| The concentration of CO_2 and NO_3^- at the catalyst-electrolyte interface in three models.

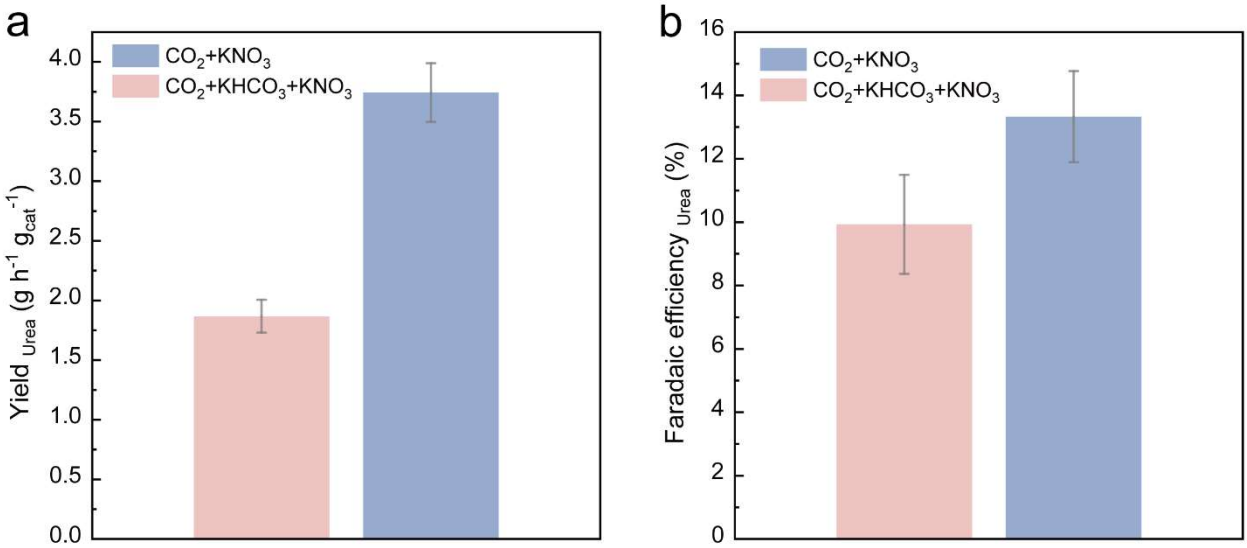

Supplementary Fig. S38| Yield rate and FE of CuRu/MCHS in different electrolytes. a, Urea yield rate and **b** FE of CuRu/MCHS at –1.1 V (vs. RHE) in CO_2-saturated 0.1 M KNO_3 and 0.1 M $KHCO_3$ + 0.1 M KNO_3 electrolytes.

Supplementary Tables

Supplementary Table S1| The ICP-OES data (wt%) of catalyst.

Samples	Cu	Ru
CuRu/MCHS-7	31.27	2.43
CuRu/CS	32.61	2.42
CuRu/MCHS-4	30.25	2.36
CuRu/MCHS-11	31.52	2.40

Supplementary Table S2| Summary of the BET surface area and porosity parameter of catalyst power.

Samples	S_{BET} (m^2 g^{-1})	Average pore diameter $_{BJH}$ (nm)	Pore volume $_{BJH}$ (cm^3 g^{-1})
MCHS-4	1298.836	4.48	1.456
MCHS-7	1495.459	7.82	1.956
MCHS-11	1091.372	12.23	1.148
CuRu/MCHS-4	647.087	4.18	0.699
CuRu/MCHS-7	721.663	7.55	0.944
CuRu/MCHS-11	654.029	11.12	0.928

Supplementary Table S3| The data of the diameter the thickness of catalysts measured from TEM images.

Samples	Hollow cavity diameter (nm)	Carbon shell thickness (nm)
CuRu/MCHS-4	228±2	19.2±0.8
CuRu/MCHS-7	214±4	52.0±1.9
CuRu/MCHS-11	202±3	53.0±1.2

Supplementary Table S4| The path parameters of the EXAFS fitting.

Sample	Space group	Cell parameter
Cu	Fm-3m	A=B=C=3.58 α=β=γ=90°
Cu_2O	Pn-3m	A=4.25, B=C=4.25 α=β=γ=90°
fcc Ru	Fm-3m	A=B=C=3.79 α=β=γ=90°
hcp Ru	P6_3/mmc	A=B=2.70, C=4.27 α=β=90°, γ=120
$CuRu_3$	I4/mmm	A=B=3.72, C=7.85 α=β=γ=90°
Cu_3Ru	P6_3/mmc	A=B=5.26, C=4.21 α=β=90°, γ=120
RuC	F-43m	A=B=C=4.56 α=β=γ=90°

Supplementary Table S5| Curve fit Parameters for Cu and Ru K-edge for CuRu/MCHS-7 and CuRu/CS.

Sample	Fitting	Path	*C.N.*	R (Å)	$\sigma^2\times10^3$ (Å^2)	ΔE_0 (eV)	R factor
CuRu/MCHS-7	Cu	Cu-O	2.16±0.60	1.88	4.8±3.0	7.46±2.30	0.0045
		Cu-Cu	4.84±0.80	2.56	9.4±1.3		
	Ru-1	Ru-C	5.02±0.75	2.03	6.8±1.4	2.08±1.81	0.0086
		Ru-Ru	1.63±0.53	2.68	6.4±2.0		
	Ru-2	Ru-O	3.02±0.51	1.97	6.8±1.5	0.53±1.52	0.0083
		Ru-Ru	2.28±0.63	2.68	9.0±1.6		
CuRu/CS	Cu	Cu-O	0.05±0.06	1.80	-15.5±5.7	7.47±1.45	0.0047
		Cu-Cu	7.96±1.09	2.56	9.8±1.1		
	Ru-1	Ru-C	5.27±0.36	2.05	7.6±0.7	0.12±0.78	0.0016
		Ru-Ru	2.89±1.05	2.69	6.5±0.7		
	Ru-2	Ru-O	3.36±0.93	1.99	8.8±2.9	1.15±2.34	0.024
		Ru-Ru	2.89±1.05	2.69	9.1±2.2		

S_0^2 was fixed as 0.87 in Cu K-range,0.95 in Ru K-range.

Supplementary Table S6| The TOF of $Cu_{24}Ru_2$/MCHS, $Cu_{24}Ru_1$/MCHS, $Cu_{24}Ru_{0.5}$/MCHS.

Samples	Yield rate ($g\ h^{-1}\ g_{cat}^{-1}$)	TOF (Cu+Ru) ($\times 10^{-2}\ s^{-1}$)
$Cu_{24}Ru_2$/MCHS	2.154	0.185
$Cu_{24}Ru_1$/MCHS	3.743	0.338
$Cu_{24}Ru_{0.5}$/MCHS	2.977	0.274

* The turnover frequency (TOF) are calculated as $TOF_{urea} = \frac{n_{urea}}{t \times n_{cat.}}$, where $n_{cat.}$ is the total loading amount of catalysts, n_{urea} is the amount of urea, and t is the reaction time.
** The average urea yield was used to calculate the TOF.

Supplementary Table S7| The ICP-MS data (μg L^{-1}) of the electrolyte after electro-catalysis test.

Elements	Cu	Ru
CuRu	120.24	3.94
	121.23	4.02
	122.22	4.01

Supplementary Table S8| A comparison of urea FEs and production rate of urea between hybrid catalysts and state-of-the-art metal and carbon based catalysts in literature.

Catalysts	Cell type	Electrolyte	Catalyst loading (mg cm^{-2})	Yield rate (g h^{-1} g_{cat}^{-1})	FE (Voltage) (%)	j_{Urea} (mA cm^{-2})	Ref.
F-doped CNT	H-cell	0.1 M KNO_3	0.10	0.382	18 (-0.65 V vs. RHE) ~3 (-0.85 V vs. RHE)	0.3	2
VB12-CNT	H-cell	0.1 M KNO_3	0.30	0.164	26.04 (-0.5 V vs. RHE) ~10 (-0.8 V vs. RHE)	~0.32	3
Nitrogen-doped carbon	H-cell	0.1 M KNO_3+0.1 M $KHCO_3$	0.15	0.596	62 (-0.3 V vs. RHE) ~5 (-0.7 V vs. RHE)	~ 0.7	4
Diatomic Fe-Ni	H-cell	0.05 M KNO_3+0.1 M $KHCO_3$	0.20	1.21	17.8 (-1.5 V vs. RHE) ~8 (-1.6 V vs. RHE)	~ 11.5	5
AuPd nanoalloy	H-cell	0.025 M KNO_3+0.075 $KHCO_3$	0.24	0.204	15.6 (-0.4 V vs. RHE)	~0.7	6
$Cu_{97}In_3$-C	H-cell	0.01 M KNO_3+0.1 M $KHCO_3$	0.20	0.786	5 (-1.5 V vs. RHE)	~1.25	7
Cu@Zn nanowires	H-cell	0.1 M KNO_3+0.2 M $KHCO_3$	NA	0.437 g h^{-1} cm^{-2}	9.28 (-1.02 V vs. RHE) ~4.5 (-1.85 V vs. RHE)	3.13	8
PdCu/CBC	H-cell	0.05 M KNO_3	0.25	0.76	58.7 (-0.4 V vs. RHE) ~10 (-0.7 V vs. RHE)	~1.17	9
3D Zn/Cu hybrid catalyst	Flow cell	0.02 M KNO_3	~2.00	3.57	63 (-0.6 V vs. RHE) ~35 (-0.9 V vs. RHE)	NA	10
Pd_4Cu_1-$Ni(OH)_2$	Flow cell	0.1 M KNO_3+0.1 M $KHCO_3$	0.10	3.628	64.4 (-0.5 V vs. RHE)	2.30	11
Cu-W bimetallic	H-cell	0.1 M KNO_3	1.00	0.098	70.1 (-0.2 V vs. RHE) ~5 (-0.5 V vs. RHE)	0.71	12
Ru-Cu copper foam	Single-cell	0.1 M $NaNO_3$	NA	0.151 g h^{-1} cm^{-2}	25.4 (0.13 V vs. RHE)	~2.50	13

CuCo diatomic catalyst	H-cell	0.1 M KNO_3+0.1 M $KHCO_3$	NA	0.89	44.04 (-0.35 V vs. RHE) ~5 (-0.75 V vs. RHE)	~0.13	14
SnBi nanosheets/rGO	Flow cell	0.1 M KNO_3+0.1 M $KHCO_3$	0.10	0.46	78.36 (-0.4 V vs. RHE) ~7 (-0.55 V vs. RHE)	~0.35	15
CuAu/CeO_2	H-cell	0.1 M KNO_3	0.10	0.813	45.2 (-0.74 V vs. RHE) ~21 (-1.0 V vs. RHE)	~0.5	16
Ru-Cu_9Bi/CNT	H-cell	0.1 M KNO_3+0.1 M $KHCO_3$	0.10	2.4	74.8 (-0.4 V vs. RHE) ~8 (-0.7 V vs. RHE)	~2.2	17
$CuPd_1Rh_1$ diatomic alloy	Flow cell	0.1 M KNO_3+0.1 M $KHCO_3$	0.50	3.19	72.1 (-0.5 V vs. RHE) ~20 (-0.7 V vs. RHE)	~10.81	18
FeCu bimetallic clusters	H-cell	0.1 M KNO_3	0.20	1.024	39.8 (-0.5 V vs. RHE) ~17 (-0.7 V vs. RHE)	0.74	19
FeN_4/B_2CuN_2@NC	H-cell	0.1 M KNO_3+0.1 M $KHCO_3$	~0.10	2.073	71.9 (-0.4 V vs. RHE) ~5 (-0.7 V vs. RHE)	1.5	20
Au@cpCu_7CF	H-cell	8 mM KNO_3+0.2 M $KHCO_3$	0.25	0.126	55.53 (Pulse potential: -0.2/-0.6 V vs. RHE)	NA	21
Rh_1Co	Flow cell	0.1 M KNO_3+0.1 M $KHCO_3$	~0.50	1.495	51.1 (-0.6 V vs. RHE) ~15 (-0.8 V vs. RHE)	~2.56	22
CuRu-CBC	H-cell	0.1 M KNO_3	1.00	0.394	68.94 (-0.55 V vs. RHE) ~18 (-0.65 V vs. RHE)	~2.76	23
Rh_1Cu	H-cell	0.1 M KNO_3+0.1 M $KHCO_3$	0.50	1.219	62.96 (-0.6 V vs. RHE)	~3.77	24
	Flow cell	0.1 M KNO_3+0.1 M $KHCO_3$	0.50	3.024	67.1 (-0.6 V vs. RHE)	~8.05	
$Ag_{14}Pd$	Flow cell	200 ppm NO_3–N+1 M KOH	NA	0.143	15.8 (-0.276 V vs. RHE) ~3 (-0.576 V vs. RHE)	~0.63	25

Cu_1Ru	Flow cell	0.1 M KNO_3+0.1 M $KHCO_3$	0.50	1.263	51.27 (-0.6 V vs. RHE) ~30 (-0.8 V vs. RHE)	~6.15	26
α-CuZn alloy	Flow cell	0.02 M KNO_3+0.2 M $KHCO_3$	0.01	3.6	28.7% (-0.42 V vs. RHE) ~10% (-0.62 V vs. RHE)	~1.44	27
CuRu/MCHS-7	H-cell	0.1 M KNO_3	0.20	3.6 (–1.1 V vs. RHE)	16.5±1.2 (-1.1 V vs. RHE)	7.5	This work
	Flow cell		0.18	5.9 (–1.1 V vs. RHE)	19.4 ± 4.5 (-1.0 V vs. RHE)	16.78	
	Flow cell (250 mA cm^{-2})		0.18	12.5	6.4	16.07	

* "~" observed or calculated from research data.

* "NA" represents not available.

Supplementary Table S9| The assignment of intermediates.

Assignment	Band center (cm^{-1})	Reference
*OCO	~1408	Adv. Funct. Mater. 2024, 34, 2400892 ACS Energy Lett. 2019, 4, 3, 682–689 J. Am. Chem. Soc. 2017, 139, 44, 15664–15667 ACS Catal. 2017, 7, 1, 606–612
*COOH	~1395	ACS Catal. 2017, 7, 606-612 Adv. Funct. Mater. 2021, 2104243 Angew. Chem. Int. Ed. 2022, 61, e20211391842
*CO	~2050	ACS Nano 2022, 16, 9095-9104 ACS Catal. 2020, 10, 15, 8049–8057
*NO	~1890	J. Am. Chem. Soc. 2022, 144, 11530-11535 ACS Catal. 2023, 13, 14, 9550–9557 Inorg. Chem. 2024, 63, 45, 21387–21396
*NH_2	~1177-1170	Angew. Chem. Int. Ed. 2024, 63, e202402215 Angew. Chem. Int. Ed. 2025, 64, e202414392 Nat. Sustain. 2021, 4, 868–876
*NH_2	~3345-3350	Angew. Chem. Int. Ed. 2025, 64, e202413534
C-N	~1425	Nat. Commun. 2024, 15, 176
N-C-N	~1477	Nat. Commun. 2024, 15, 176

Supplementary Table S10| The calculated Δ*E*, ΔE_{ZPE} and TΔ*S* of various species along the reaction pathways for urea synthesis on the CuRu model.

Species	Δ*E* (eV)	ΔE_{ZPE} (eV)	*T*Δ*S* (eV)
HNO_3	-28.59	0.71	0.35
*CO_2	-1111.39	0.28	0.35
*COOH	-1115.20	0.60	0.38
*CO_2NO	-1126.15	0.53	0.45
*CO_2NHO	-1131.06	0.88	0.46
*CO_2NHOH	-1134.75	1.19	0.51
*CO_2NH	-1125.32	0.76	0.34
*CO_2NH_2	-1129.45	1.11	0.41
*$COOHNH_2$	-1132.78	1.39	0.51
*$CONH_2$	-1120.86	0.94	0.36
*$ONCONH_2$	-1135.95	1.23	0.41
*$CO(NH_2)$	-1137.96	1.77	0.44
*CO_2+*NO	-1126.71	0.50	0.65
*CO_2+*NHO	-1131.21	0.79	0.70
*CO_2+*NHOH	-1135.58	1.09	0.71
*CO_2+*NH	-1125.76	0.66	0.49
CO_2+NH_2	-1130.19	0.98	0.52
COOH+NH_2	-1133.12	1.27	0.68

Supplementary Table S11| The calculated free energy barriers of *COOH-NH_2 and *OCO-NO pathways for urea synthesis on the CuRu model.

Reaction coordinates	ΔG (eV)
*CO_2+*NO → *CO_2NO	+0.79
*CO_2NH_2 → *CO_2NO	+0.33
CO_2+NH_2 → *COOH+*NH_2	+0.67
COOH+NH_2 →*$COOHNH_2$	+0.64

Supplementary Table S12| The calculated Δ*E*, ΔE_{ZPE} and TΔ*S* of various species along the reaction pathways for urea synthesis on the Cu model.

Species	Δ*E* (eV)	ΔE_{ZPE} (eV)	*T*Δ*S* (eV)
*CO_2	-1088.34	0.28	0.35
*COOH	-1091.85	0.60	0.38
*CO_2NO	-1101.90	0.50	0.49
*CO_2NHO	-1106.45	0.84	0.51
*CO_2NHOH	-1110.58	1.16	0.66
*CO_2NH	-1101.16	0.76	0.40
*CO_2NH_2	-1105.58	1.08	0.53
*$COOHNH_2$	-1108.72	1.38	0.57
*$CONH_2$	-1097.49	0.95	0.42

Supplementary Table S13| Parameters for finite element simulation modeling.

Samples	Pore diameter (nm)	Hollow cavity diameter (nm)	Carbon shell thickness (nm)
CuRu/MCHS-4	4	200	10
CuRu/MCHS-7	7	200	20
CuRu/MCHS-11	11	200	20

Supplementary Table S14| Diffusion coefficients of solution species[28].

Solution species	Diffusion coefficient ($m^2 s^{-1}$)
K^+	1.957×10^{-9}
Cl^-	1.185×10^{-9}
H^+	9.311×10^{-9}
CO_2	1.910×10^{-9}
OH^-	5.273×10^{-9}
NO_3^-	1.902×10^{-9}
NH_4^+	1.957×10^{-9}
Urea	2.92×10^{-9}
NO	2.53×10^{-9}
H_2	4.5×10^{-5}

References

1 Anker, S. *et al.* Assessment of GAFF and OPLS force fields for urea: crystal and aqueous solution properties. *Cryst. Growth Des.* **24**, 143–158 (2024).

2 Liu, X. *et al.* Carbon nanotubes with fluorine-rich surface as metal-free electrocatalyst for effective synthesis of urea from nitrate and CO_2. *Appl. Catal. B Environ.* **316**, 121618 (2022).

3 Cong, M. Y. *et al.* Electrocatalytic urea synthesis from CO_2 and nitrate co-reduction on natural vitamin B12 coupled carbon nanotubes. *Appl. Catal. B Environ.* **351**, 123941(2024).

4 Li, Y. *et al.* Sequential co-reduction of nitrate and carbon dioxide enables selective urea electrosynthesis. *Nat. Commun.* **15**, 176 (2024).

5 Zhang, X. *et al.* Identifying and tailoring C–N coupling site for efficient urea synthesis over diatomic Fe–Ni catalyst. *Nat. Commun.* **13**, 5337 (2022).

6 Wang, H. *et al.* Realizing efficient C–N coupling via electrochemical co-reduction of CO_2 and NO_3^- on AuPd nanoalloy to form urea: key C–N coupling intermediates. *Appl. Catal. B Environ.* **318**, 121819 (2022).

7 Liu, Y. *et al.* C-bound or O-bound surface: Which one boosts electrocatalytic urea synthesis? *Angew. Chem. Int. Ed.* **62**, e202300387 (2023).

8 Meng, N. *et al.* Oxide-derived core-shell Cu@Zn nanowires for urea electrosynthesis from carbon dioxide and nitrate in water. *ACS Nano* **16**, 9095–9104 (2022).

9 Zhang, S. *et al.* High-efficiency electrosynthesis of urea over bacterial cellulose regulated Pd–Cu bimetallic catalyst. *EES Catal.* **1**, 45–53 (2023).

10 Luo, Y. *et al.* Selective electrochemical synthesis of urea from nitrate and CO_2 via relay catalysis on hybrid catalysts. *Nat. Catal.* **6**, 939–948 (2023).

11 Xu, M. *et al.* Kinetically matched C–N coupling toward efficient urea electrosynthesis enabled on copper single-atom alloy. *Nat. Commun.* **14**, 6994 (2023).

12 Zhao, Y. *et al.* Efficient urea electrosynthesis from carbon dioxide and nitrate via alternating Cu–W bimetallic C–N coupling sites. *Nat. Commun.* **14**, 4491 (2023).

13 Qin, J. Z. *et al.* Selective electrochemical urea synthesis from nitrate and CO_2 in situ Ru anchoring onto a three-dimensional copper electrode. *ACS Sustain. Chem. Eng.* **10**, 15869–15875 (2022).

14 Lv, Z. *et al.* CuCo DAC used to change the hydrogenation sequence for efficient electrochemical C–N coupling. *Appl. Catal. B Environ.* **351**, 124003 (2024).

15 Chen, X. Y. *et al.* Amorphous bismuth-tin oxide nanosheets with optimized C–N coupling for efficient urea synthesis. *J. Am. Chem. Soc.* **146**, 13527–13535 (2024).

16 Zhan, P. *et al.* Efficient electrosynthesis of urea over single-atom alloy with electronic metal support interaction. *Angew. Chem. Int. Ed.* **63**, e202409019 (2024).

17 Yu, Y. *et al.* Achieving efficient urea electrosynthesis through improving the coverage of a crucial intermediate across a broad range of nitrate concentrations. *Energy Environ. Sci.* **17**, 5183–5190 (2024).

18 Chen, K. *et al.* Urea electrosynthesis from nitrate and CO_2 on diatomic alloys. *Adv. Mater.* **36**, 2402160 (2024).

19 Hou, T. *et al.* FeCu bimetallic clusters for efficient urea production via coupling reduction of carbon dioxide and nitrate. *J. Colloid Interface Sci.* **674**, 834–840 (2024).

20 Zhou, M. *et al.* Tailoring O-monodentate adsorption of CO_2 initiates C−N coupling for efficient urea electrosynthesis with ultrahigh carbon atom economy. *Angew. Chem. Int. Ed.* **64**, e202414392 (2025).

21 Zhang, X. *et al.* Dynamic control of asymmetric charge distribution for electrocatalytic urea synthesis. *Adv. Mater.* **36**, 2408510 (2024).

22 Wan, Y. Y. *et al.* Single-atom Rh alloyed Co for urea electrosynthesis from CO and NO. *Nano Lett.* **24**, 10928–10935 (2024).

23 Liu, J. F. *et al.* Ambient electrosynthesis of urea with nitrate and carbon dioxide over a CuRu alloy catalyst. *Chem. Commun.* **60**, 11592–11595 (2024).

24 Xiang, J. Q. *et al.* Relay catalysis of isolated rhodium-alloyed copper boosts urea electrosynthesis from nitrate and CO. *ACS Nano* **18**, 29856–29863 (2024).

25 Chen, H. *et al.* Atomically precise silver-based bimetallic clusters for electrocatalytic urea synthesis. *Nat. Sci. Rev.* **12**, nwae440 (2024).

26 Wang, F. Z. *et al.* Selective urea electrosynthesis from nitrate and CO on isolated copper alloyed ruthenium. *ACS Energy Lett.* **9**, 4624–4632 (2024).

27 Zhai, S. et al. Brass phase determining selectivity in urea electrosynthesis from CO_2 and nitrate. *ACS Catal.* 15, 3276-3283 (2025).

28 Rumble, J., CRC Handbook of chemistry and physics. 100th ed.; CRC Press: (2019).